Chapter 2
Factors Affecting the Bulk Embrittlement of Pb-Free Solder Joints

K. Lambrinou

Abbreviations

ASTM	American Society for Testing and Materials
bcc	Body-centred cubic
bct	Body-centred tetragonal
BSE	Back scattered electron
CAT	Crack-arrest temperature
CMOD	Crack-mouth opening displacement
CTOD	Crack-tip opening displacement
CVN	Charpy V-notch
DBTT	Ductile-to-brittle transition temperature
fcc	Face-centred cubic
FTE	Fracture transition elastic temperature
FTP	Fracture transition plastic temperature
hcp	Hexagonal close-packed
IMC(s)	Intermetallic(s) or intermetallic compound(s)
LLD	Load line displacement
NDT	Nil ductility temperature
Pb-free	Lead-free
SAC	Sn–Ag–Cu
SE	Secondary electron
SEM	Scanning electron microscopy
Sn-based	Tin-based

K. Lambrinou
IMEC, Kapeldreef 75, 3001 Leuven, Belgium

Present Address:
K. Lambrinou (✉)
SCK-CEN, Boeretang 200, 2400 Mol, Belgium
e-mail: klambrin@sckcen.be

G. Grossmann and C. Zardini (eds.), *The ELFNET Book on Failure Mechanisms, Testing Methods, and Quality Issues of Lead-Free Solder Interconnects*,
DOI: 10.1007/978-0-85729-236-0_2,

Special Symbols

[]* Figure adapted from the reference given in []

[]§ From "The Science and Engineering of Materials", 5th edition, by Askeland and Phulé. © 2006 by Nelson. Reprinted with permission of Nelson, a division of Thomson Learning: www.tomsonrights.com. Fax: 800 730 2215

[]# From "The Science and Engineering of Materials", 1st edition, by Askeland. © 1984 by Wadsworth, Inc. Reprinted with permission of Brooks/Cole, a division of Thomson Learning: www.tomsonrights.com. Fax: 800 730 2215

[]& From "Deformation and Fracture Mechanics of Engineering Materials", 4th edition, by Hertzberg. © 1996 by John Wiley & Sons, Inc. Reprinted with permission of John Wiley and Sons, Inc

[]† From "Fracture and Fatigue Control in Structures: Applications of Fracture Mechanics", 3rd edition, by Barsom and Rolfe. © 1999 by ASTM International. Reprinted with permission of ASTM International

[]∝ Reproduced with permission of Emerald Group Publishing Ltd. © 2000 by MCB University Press

2.1 Introduction

The fracture behaviour of all materials is affected by several factors, some of which are 'intrinsic', i.e. reflecting the material constitution, and some 'extrinsic', i.e. relating to the processing or service conditions. Examples of 'intrinsic' factors are the material composition, crystal structure, and microstructure, while examples of 'extrinsic' factors include the cooling rate during processing, as well as the temperature, strain rate, or constraint of the material during service. Changes in the processing or service conditions often alter the crystal structure, microstructure, or even composition of the material (e.g. by contamination), which might affect its fracture behaviour. Electronic materials, like the lead-free (Pb-free) solders studied in the framework of ELFNET, are no exception to the above general rules of thumb. It has already been observed, for example, that the fracture behaviour of tin-based (Sn-based) solders changes from ductile to brittle under solder-specific service conditions. This type of brittle fracture occurs in the solder joint unlike the typical brittle failures occurring in the intermetallic layers that are present between solder joint and bond pad; therefore, it is often referred to as 'bulk solder embrittlement'. This chapter attempts to identify the factors affecting the bulk embrittlement of Sn-based Pb-free solder joints, as this type of embrittlement may occur during the solder joint life cycle, depending on the requirements of the 'mission profile'. Identifying these factors and understanding how they facilitate embrittlement is the first step in finding ways to limit, delay, or even avoid bulk solder joint embrittlement during service. However, due to the limited available data, the factors affecting the bulk embrittlement of Pb-free solder joints will be addressed by referring to data acquired from studying other metallic materials with similar behaviour, e.g. ferritic steels.

2.1.1 Comparing Ductile to Brittle Fractures

It is common knowledge that *brittle fractures* occur with little or no plastic deformation prior to failure and are characterised by very limited energy absorption. This is the type of failure that occurs at extremely high speeds (up to 2,000 m/s or 7,000 ft/s in steels) [1]. An example of the stress–strain behaviour of a brittle material subjected to tension is given in Fig. 2.1a, where one may observe the essential absence of strain (i.e. deformation) before failure of the material at the ultimate tensile strength, σ_{tens}.

Contrary to brittle fractures, ductile fractures are characterised by appreciable plastic deformation prior to failure and high energy consumption [1]. When a ductile material is subjected to tension, as shown in Fig. 2.1b, an appreciable amount of strain usually results from loading the material above its yield strength, σ_{yield}. The fact that ductile materials deform a lot before failing, and that this failure is relatively slow, makes ductile fractures more appealing than brittle ones in the eyes of the design engineer.

Two notions very closely related to the type of material failure (i.e. ductile vs. brittle) are those of toughness and ductility. *Toughness* is the ability of a material to resist fracture and represents the energy absorbed during failure [2, 3]. A brittle material, for example, absorbs small amounts of energy during fracture, while a tough/ductile material absorbs large energy amounts. For an unnotched tensile bar, the energy dissipated during failure can be estimated from the area under the stress–strain curve (Fig. 2.1), as follows [2]:

$$\text{Energy/volume} = \int_0^{\varepsilon_f} \sigma d\varepsilon \tag{2.1}$$

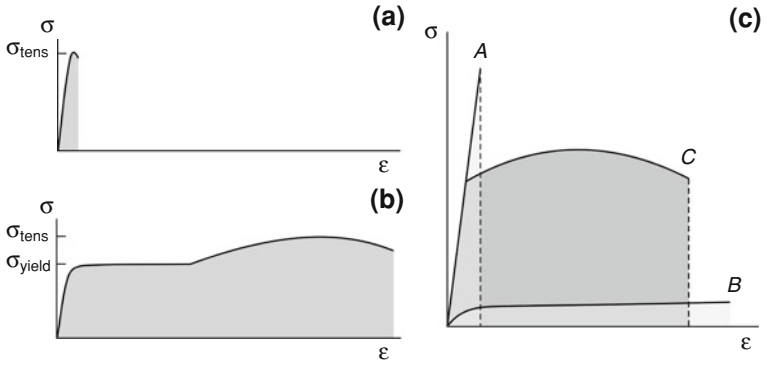

Fig. 2.1 Typical stress–strain curves of (**a**) brittle materials and (**b**) ductile materials [1]*. **c** Superposition of the stress–strain curves of a strong material with little capability for plastic flow (*A*), a material with low strength but high ductility (*B*), and a material with optimum combination of strength and ductility for maximum toughness (*C*) [2]*. * Figure adapted from the Reference in []. The meaning of symbol * is the same throughout this text

where σ is the stress, ε is the strain, and ε_f is the strain at failure.

On the other hand, *ductility* is the ability of a material to deform plastically without fracturing. Ductility is commonly expressed either as % elongation in the gage length, or % reduction in the area of a tensile specimen tested to failure [4]. It must be emphasised that maximum toughness requires a combination of strength and ductility [2], since high strength or good ductility alone cannot guarantee an enhanced toughness (Fig. 2.1c).

2.1.2 Factors Affecting the Type of Fracture

It is often erroneously believed that the type of fracture of a certain material is either ductile or brittle and that defining the fracture type is quite straightforward. This could, for example, be based on the fact that the deformation and fracture characteristics of materials depend on very material-specific properties, such as the nature of the electron bond, the crystal structure, and the degree of atomic order [2]. Another way to predict the type of failure of a material would be to consider its fundamental engineering properties, such as the yield strength, tensile strength, and tensile ductility [2], since high-toughness materials combine good strength and ductility. However, the job of a design engineer is not that simple, because some materials (like many metals) that fail in a ductile manner under mild service conditions might embrittle if subjected to low temperatures, high strain rates, or multiaxial stress states related to the presence of notches or defects [1–3]. The Sn-based Pb-free solders extensively addressed in this chapter fall into that category, for example. Moreover, some materials (like many ceramics) that fail in a brittle manner at mild ambient temperatures will certainly increase their ductility when exposed to sufficiently high temperatures; for ceramics, this change in fracture behaviour occurs usually above 1,000°C [5].

2.2 Crystal Structure, Microstructure, and Fracture Resistance

As mentioned in Sect. 2.1.2, the deformation and fracture characteristics of a material are affected by the nature of the electron bond, the crystal structure, and the degree of atomic order in the material. For example, the more rigidly fixed the valence electrons, the greater the propensity of a material to fail in a brittle manner [2]. In ionic solids, the valence electrons are tightly bound to their respective atoms inside the crystal [6], which explains their high propensity to brittle failure. In both covalent and metallic crystals, the valence electrons are shared between atoms [6]; however, their fracture behaviour is different due to the following reasons: in covalent solids, the valence electrons are shared between an

atom and its nearest neighbours, while in metallic solids, the valence electrons are shared equally by all atoms in the material. The greater restriction in the movement of valence electrons experienced by covalent materials (e.g. diamond, silicon, carbides, nitrides, and silicates) accounts for their tendency to fail in a brittle manner, while materials held together by metallic bonds are the easiest to deform, failing usually in a ductile manner [2].

Materials with a low crystal symmetry, where slip is difficult, show a greater tendency to fail in a brittle manner. On the contrary, close-packed crystals characterised by high crystal symmetry are capable of considerable plastic deformation. For example, *face-centred cubic (fcc)* and *hexagonal close-packed (hcp)* crystals are less prone to brittle failure than *body-centred cubic (bcc)* crystals. Moreover, bcc metals show a much higher propensity to low-temperature embrittlement than fcc and hcp metals, as will be discussed more extensively later on. Figure 2.2 shows schematic representations of the fcc, bcc, and hcp crystal structures.

Another structural factor that affects the fracture resistance of a material is the degree of order in the atomic arrangement. It has been observed that the tendency for brittle failure increases as the degree of order in the atomic arrangement increases. In fact, the addition of a solute to a crystal lattice progressively suppresses plastic flow, as the solid solution that results from this addition changes gradually from disordered to short-range ordered first, and subsequently to long-range ordered [2].

The above-discussed theoretical aspects of the material structure have a great impact on the material's fracture resistance, but might be difficult to grasp and put

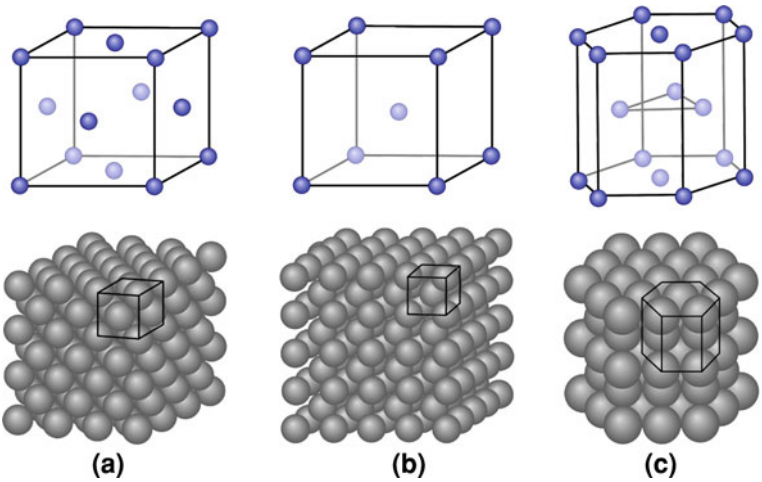

Fig. 2.2 **a** The face-centred cubic (fcc) crystal structure is shown as a reduced-sphere unit cell and an atomic aggregate [5]*. **b** The body-centred cubic (bcc) crystal structure is shown as a reduced-sphere unit cell and an atomic aggregate [5]*. **c** The hexagonal close-packed (hcp) crystal structure is shown as a reduced-sphere unit cell and an atomic aggregate [5]*

in practice by the design engineer. A simple question remains: What are the practical ways one could use to limit the tendency for brittle failure of a structural material? And if embrittlement cannot be avoided, as often happens at extreme service conditions, what are the available testing methods that can provide accurate information on the limitations of a specific material?

2.2.1 Elements of Fracture Mechanics

Before attempting to answer the above critical questions, it would be useful to introduce and put into perspective the following two concepts: (a) the stress-intensity factor and (b) the fracture toughness. It is common knowledge that the materials used to build any structure are not perfect, since they contain cracks, sharp notches, and discontinuities of various kinds. These defects create stress concentrations within the material, increasing its tendency to failure. Therefore, the design engineer needs a tool that allows the quantitative determination of the allowable stress levels in such structures, so as to avoid fracture during service. This tool is the scientific discipline of Fracture Mechanics, which envisages the intensity of stress concentration as the *driving force* to failure, and the material's fracture toughness as the *resistance force* against failure [1].

Depending on the mode of loading, the fracture of flaw-containing components may be described by a stress analysis based on principles of elasticity theory. Figure 2.3 illustrates the three major modes of loading, which are [1, 2]:

1. *Mode I*: the opening or tensile mode, where the crack surfaces move directly away from each other,
2. *Mode II*: the sliding or in-plane shear mode, where the crack surfaces slide over one another in a direction perpendicular to the crack leading edge, and
3. *Mode III*: the tearing or anti-plane shear mode, where the crack surfaces also move relative to one another, but in this case parallel to the crack leading edge. Since mode I loading is the most frequently encountered in structural applications involving cracked components, both the stress-intensity factor and the fracture toughness are defined with respect to that loading mode in the present text.

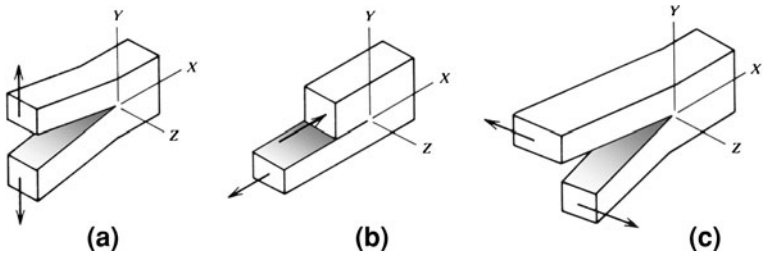

Fig. 2.3 The three basic loading modes: **a** Mode I, **b** Mode II, and **c** Mode III [1, 2]*

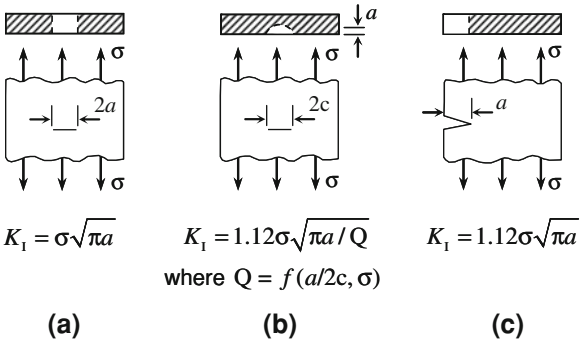

Fig. 2.4 Equations relating the stress-intensity factor, K_I, with the stress, σ, and the crack size, a, for the following crack configurations: **a** through-thickness crack, **b** surface crack, and **c** edge crack. These equations describe the elastic-stress field in the vicinity of a crack tip inside a body subjected to tension [1]*

In linear-elastic fracture mechanics, the stress field ahead of a sharp crack subjected to mode I loading is characterised by the *stress-intensity factor*, K_I, which has units of MPa$\sqrt{\text{m}}$ or ksi$\sqrt{\text{in.}}$ [1]. This parameter is related to both the stress level, σ, and the flaw size, a. Figure 2.4 provides equations describing the elastic-stress field near the tip of cracks with different configurations, inside a body stressed in tension. In summary, K_I is affected by the specimen geometry, the applied load, as well as the size and shape of the flaw [1]. When the combination of σ and a results in a critical K_I value, unstable crack growth (related to brittle failure) occurs. This critical value of the stress-intensity factor at failure, K_{Ic}, is the so-called *fracture toughness*, and it is a material property [1]. The fracture toughness represents the resistance of a certain test specimen against crack propagation. It must be emphasised, however, that determining the fracture toughness of a structural material is not always an easy task, as the fracture toughness is influenced by the service temperature, loading rate, and degree of material constraint. Therefore, the K_{Ic} of a certain material can be determined for a specimen with a given thickness at a specified temperature and loading rate. In general, the fracture toughness decreases by decreasing the temperature, increasing the loading rate, and/or increasing the material thickness [1, 2]. Special reference will be made to each one of these factors later in the text, as they are also expected to affect the fracture behaviour of certain Pb-free solders.

2.2.2 Metallurgical Aspects of Fracture Resistance

It has already been mentioned that high toughness demands the combination of strength and ductility. However, metallurgists take this concept one step further and strive for the production of structural materials that exhibit both high strength

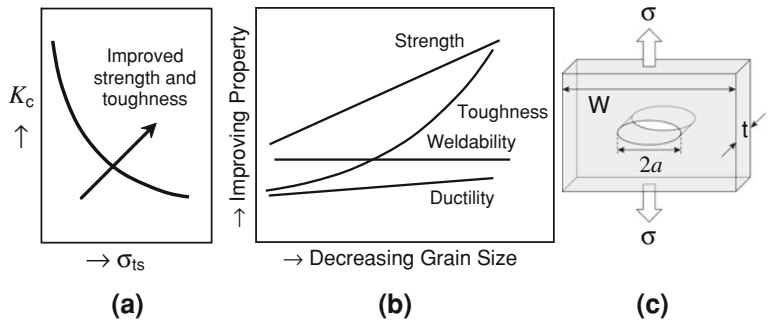

Fig. 2.5 **a** Inverse relation between the tensile strength, σ_{ts}, and the fracture toughness, K_c, of an alloy. Optimising the alloy properties would ideally result in a shift of the tensile strength–fracture toughness curve in the direction of the *arrow* [2]*. **b** Grain size refinement results in a simultaneous improvement in the strength and the toughness of the alloy. Reduction in the grain size does not affect adversely the alloy's weldability or ductility [2]*. **c** Through-thickness crack in a large plate subjected to a tensile stress σ. *W* is the plate width, t the plate thickness, and 2*a* the crack length [2]*

and fracture toughness. This is asking for a lot, since the strengthening of a material happens almost invariably at the detriment of its fracture toughness, as shown in Fig. 2.5a. Still, there are ways to improve both the strength and the fracture toughness of a material [2]; these ways should also be considered for the improvement of the in-service performance of commercially available Pb-free solders. The simultaneous improvement in strength and toughness may be achieved in one of the following ways:

1. By modifying the alloy chemistry and melting/processing process to improve the toughness; this could, for example, happen by removing or neutralising certain undesirable elements that degrade the toughness,
2. By optimising the microstructure and phase distribution to maximise the toughness, and/or
3. By refining the microstructure, or in other words, by opting for finer grain sizes.

Point (3) is quite obvious for all materials, and its effect on strength, toughness, and weldability is graphically presented in Fig. 2.5b. In order to provide a better insight into the benefits of microstructural refinement, the following could be said: strengthening occurs because smaller grains are likely to contain smaller flaws; smaller inherent flaws imply the need of a greater stress to achieve failure.

In terms of equations, Griffith [1, 2] suggested that the stress required for failure is given by:

$$\sigma = \sqrt{\frac{2E\gamma_s}{\pi a}} \quad \text{for plane-stress (biaxial stress) conditions} \tag{2.2}$$

and

$$\sigma = \sqrt{\frac{2E\gamma_s}{\pi a(1-v^2)}} \quad \text{for plane-strain (triaxial stress) conditions} \tag{2.3}$$

where E is the material's modulus of elasticity, γ_S is the specific energy of the surface created during fracture, $2a$ is the crack length, and v is the Poisson's ratio of the material. Obviously, the larger the size of the flaw/crack, the lower the stress required to fracture the material. A model crack may be visualised in Fig. 2.5c. With respect to the toughening of a single-phase material by grain refinement, one could think that the finer the grain size, the more often will a crack cross grain boundaries during its propagation. Since grain boundaries tend to decelerate or even stop cracks, the travelling crack will spend more energy to propagate in a finer-grained material than in a coarser-grained one. The higher the energy absorbed during fracture, the tougher the material.

Examples of improving the properties of Pb-free solders based on the suggestions made in points (1) and (2) include the addition of special retardants to avoid tin pest on tin-based (Sn-based) solder alloys (in relation to point 1), and/or the control of the size, shape, and acuity (i.e. sharpness) of the intermetallic (IMC) particles in the solder bulk (in relation to point 2). Reference to the last two examples will be made later in the text. Before moving to the next section, however, it would be useful to briefly underline the role of IMC particles in the in-service embrittlement of Pb-free solder alloys.

Intermetallics or *intermetallic compounds* (IMCs) are discrete chemical compounds made by the mixing, in a certain proportion, of two or more metals with each other or with non-metals [5, 7]. An example of a widely known intermetallic compound formed in steels is cementite (Fe_3C). It is quite important to realise that the structure and properties of intermetallics are different from those of the constituent metals; for example, IMCs are characterised by enhanced atomic order and mixed (metallic and covalent/ionic) bonding. Moreover, their properties are a compromise between the typical properties of ceramics and those of metals: when compared to most metals, they exhibit higher hardness and refractoriness, together with poorer toughness and workability (and, hence, ductility). It has also been shown that the presence of brittle second-phase particles in an otherwise ductile matrix is a major cause of embrittlement [2]. Figure 2.6 illustrates this principle, showing that the probability of crack initiation at particles such as the IMCs in Pb-free solders is very high. The above indicates that the presence of IMCs in the bulk of Pb-free solder alloys is a major concern when it comes to the fracture behaviour of these alloys, as will be illustrated later in the text.

2.2.3 Elements of Dislocation Theory

Dislocations are very important, especially for metals and metallic alloys, since they provide a mechanism for plastic deformation, which may be regarded as the

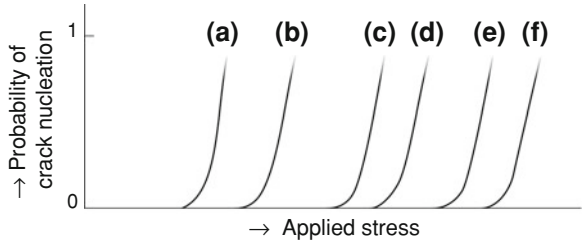

Fig. 2.6 Probability as a function of the applied stress that one of the following microcrack formation mechanisms is active: [*a*] embrittled grain boundaries, [*b*] brittle second-phase particles, [*c*] twin–twin intersections, [*d*] twin–grain boundary intersections, [*e*] slip-induced grain boundary opening (e.g. at triple points), and [*f*] slip band-slip band intersections. From a study conducted on high-purity iron-containing carbides as brittle second-phase particles [2]*

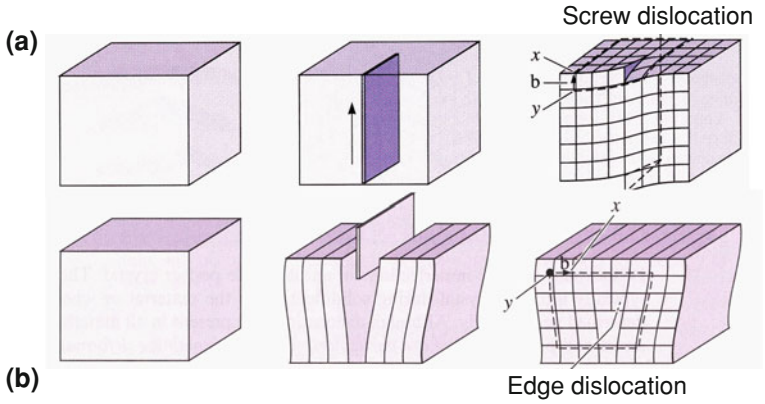

Fig. 2.7 **a** For the creation of a screw dislocation, the perfect crystal is cut and sheared one atom spacing; the screw dislocation is the line across which shearing occurs [7]§. **b** For the creation of an edge dislocation, the perfect crystal is cut and an extra plane of atoms is inserted; the edge dislocation is the bottom edge of the extra plane [7]§. In both types of dislocations, a Burgers vector (**b**) is required to close a loop of equal atom spacings around the dislocation. § From "The Science and Engineering of Materials", 5th edition, by Askeland and Phulé. © 2006 by Nelson. Reprinted with permission of Nelson, a division of Thomson Learning: www.tomsonrights.com. Fax: 800 730 2215. The meaning of symbol § is the same throughout this text

cumulative effect of the slip of numerous dislocations [7]. *Dislocations* are line imperfections in an otherwise perfect crystal, where they are usually introduced either during solidification or permanent (i.e. plastic) deformation [7]. There are three known types of dislocations: the screw dislocation, the edge dislocation, and the mixed dislocation. Figure 2.7 gives a visual impression of two of them: the screw dislocation and the edge dislocation.

Slip is the process by which a dislocation moves in a material, resulting in the deformation of this material [7]. Figure 2.8 illustrates the slip process for both an edge dislocation and a screw dislocation. Slip explains why the strength of a metal

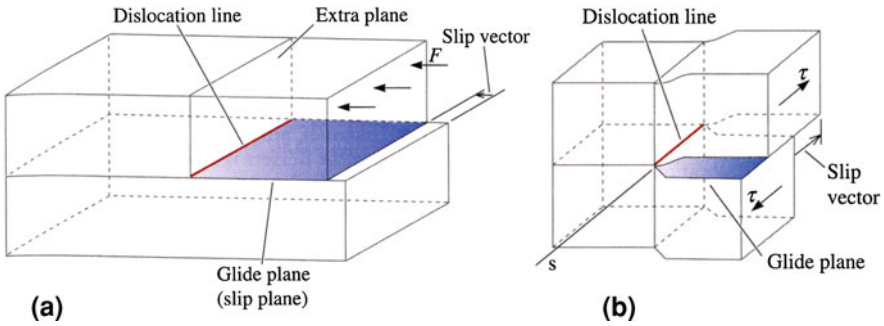

Fig. 2.8 Schematic representation of the slip line, slip plane, and slip (Burgers) vector for (**a**) an edge dislocation and (**b**) a screw dislocation [7][§]

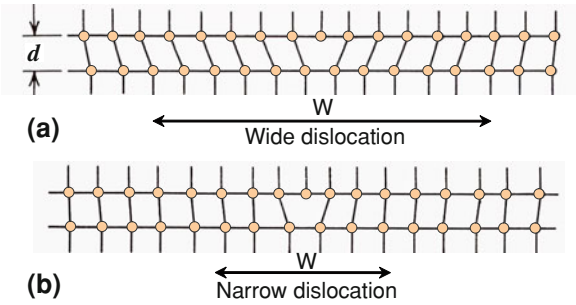

Fig. 2.9 Schematic representation of two edge dislocations with different width: (**a**) a wide edge dislocation, and (**b**) a narrow edge dislocation. *W* is the dislocation width [2]*

is much lower than the theoretical strength predicted from the metallic bond. In this sense, slip is responsible for the ductility and, therefore, the workability of metals. On the other hand, the presence of dislocations offers also the possibility of strengthening a certain metallic material by introducing obstacles (e.g. second-phase particles) that interfere with the dislocation motion [2, 8].

It has by now become clear that the movement of dislocations is a prerequisite for plastic deformation before fracture, and it should ideally occur even at extreme service conditions (e.g. low temperatures, high strain rates), if brittle failures were to be avoided. Unfortunately, the lattice resistance to dislocation movement changes with temperature, and this is the basis of the low-temperature embrittlement encountered in Sn-based Pb-free solders, which will be addressed later in the text. The resistance of a lattice to dislocation movement is expressed by the magnitude of the force required to move a dislocation through this lattice. This is known as the *Peierls–Nabarro force*, and the corresponding stress is the *Peierls–Nabarro stress* [2].

The magnitude of the Peierls–Nabarro stress decreases as the width of the dislocation, W, or the distance between similar planes, *d*, increases (Fig. 2.9). Since the interplanar spacing, *d*, increases with the planar atomic density, it is easier to have slip on close-packed planes. Moreover, the dislocation width, which

represents the distance over which the lattice is distorted due to the presence of the dislocation, is large when the bonding forces are spherical in distribution and act along the line between atomic centres. This type of bonding characterises the close-packed structures of fcc and hcp crystals. On the other hand, highly directional bonding forces, as in the case of bcc, ionic, or covalent crystals, result in narrow dislocations. Therefore, the Peierls–Nabarro stress is low in fcc and hcp crystals, moderate in bcc crystals, and large in ionic or covalent crystals (e.g. ceramic materials) [2].

The Peierls–Nabarro stress is sensitive to the lattice thermal energy and, hence, to the ambient temperature [2]. Decreasing the temperature limits the thermal energy available for dislocation motion, which increases the Peierls–Nabarro stress, especially for crystals with a high starting Peierls–Nabarro stress (e.g. bcc). However, crystals with a negligible starting Peierls–Nabarro stress (e.g. fcc and hcp) experience little increase in their Peierls–Nabarro stress when the ambient temperature decreases. It is also quite important to realise that the temperature dependence of the Peierls–Nabarro stress is related to the temperature dependence of the yield strength of a material [2]. Before going deeper into the last phenomenon, it might be useful to introduce the yield strength and the (ultimate) tensile strength of a metallic material with the help of Fig. 2.10, which shows the stress–strain curve resulting from the tensile testing of an aluminium (Al) alloy to failure. Upon stress application in the elastic regime, the material deforms elastically, which means that the strain will be completely recovered as soon as the

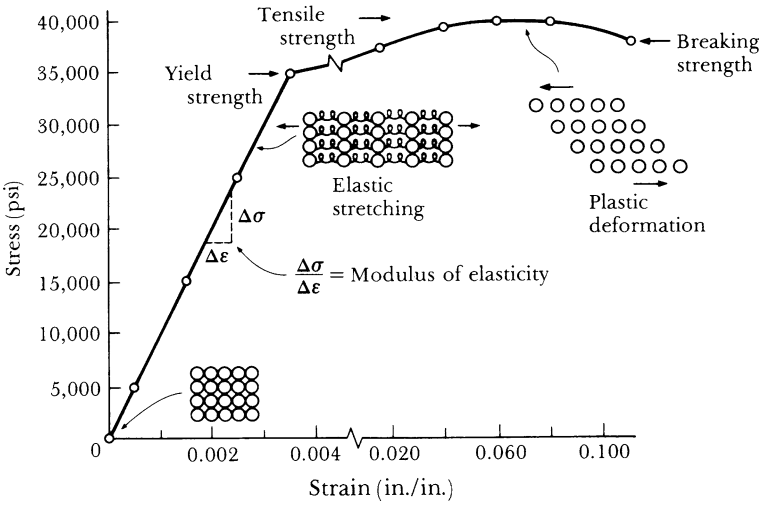

Fig. 2.10 The stress–strain curve resulting from the tensile testing of an Al alloy [9]#. # From "The Science and Engineering of Materials", 1st edition, by Askeland. © 1984 by Wadsworth, Inc. Reprinted with permission of Brooks/Cole, a division of Thomson Learning: www.tomsonrights.com. Fax: 800 730 2215. The meaning of symbol # is the same throughout this text

stress is withdrawn. The slope of the stress–strain curve in the elastic region is the material's *modulus of elasticity* or *Young's modulus*, *E*. As the applied stress increases, the material starts to deform both elastically and plastically. The critical stress value required to initiate plastic deformation is defined as the *elastic limit* of the material [3, 7]. In metallic materials, this is usually the stress required for dislocation motion or slip to be initiated. On the other hand, the stress level above which the relationship between stress and strain is not linear is the so-called *proportional limit* [3, 7]. In most materials, the elastic and proportional limits are quite close, but neither of them can be determined accurately since the measured values depend on the sensitivity of the equipment. Therefore, an *offset strain value* (typically, 0.002 or 0.2%) is defined, from which a line is drawn parallel to the linear portion of the stress–strain curve. The stress value corresponding to the intersection of this line and the stress–strain curve is the *0.2% offset yield strength* or *yield strength* [3, 7]. At stresses higher than the yield strength, plastic deformation occurs. The stress corresponding to the highest applied force is the *tensile strength* of the tested material. In ductile materials, the tensile strength is the stress at which *necking* begins. Necking refers to the formation of an area in the tensile specimen that is locally much more deformed (i.e. thinner) than the rest of the specimen.

The fact that the temperature dependence of the Peierls–Nabarro stress is related to that of the yield strength is the reason why the yield strength of fcc metals like Al, copper (Cu), and austenitic stainless steel alloys has a limited temperature dependence [2, 4, 9]. Figure 2.11a shows the temperature dependence of the tensile properties of an Al alloy [9]. This plot shows that as the temperature decreases, both the yield and tensile strength of the Al alloy increase. However, the

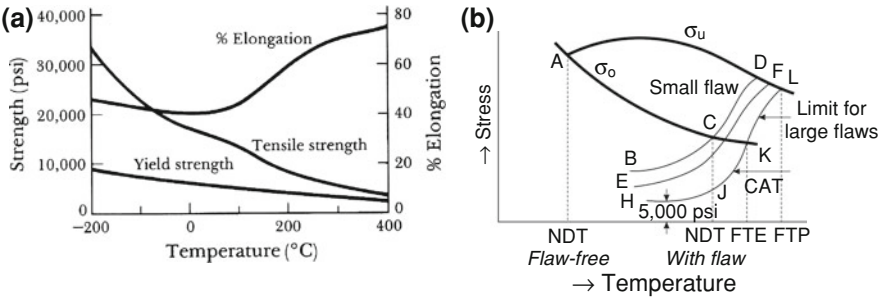

Fig. 2.11 **a** The effect of temperature on the tensile properties of an Al alloy [9]#. **b** The temperature dependence of the yield, tensile, and fracture strength (the latter is given by curves BCD, EF, and HJKL) of a steel containing flaws of various sizes. CAT is the crack-arrest temperature curve: it gives the stress required for the unstable propagation of a large flaw as a function of temperature; fracture does not occur at any point on the right of that curve. FTE is the fracture transition elastic temperature, i.e. the temperature above which elastic stresses cannot propagate a crack. Above FTP, which is the fracture transition plastic temperature, the material behaves as if it were flaw-free; this means that a crack (irrespective of its size) cannot propagate in an unstable manner [8]

yield strength increases less rapidly than the tensile strength, which allows the Al alloy to retain some of its ductility at low service temperatures. The reason for the not-so-steep increase in the yield strength with lowering the temperature is related to the limited temperature dependence of the Peierls–Nabarro stress of this alloy. Examples of other fcc metals that for the same reason remain ductile at low temperatures include nickel (Ni), lead (Pb), and silver (Ag) [4].

On the contrary, the Peierls–Nabarro stress in bcc metals like iron (Fe), chromium (Cr), molybdenum (Mo), tantalum (Ta), tungsten (W), and ferritic stainless steel alloys rises rapidly with decreasing temperature [2, 4, 9]. This happens due to the strong temperature dependence of the Peierls–Nabarro stress, which becomes a large part of the yield strength in the low-temperature regime [2]. Figure 2.11b shows the temperature dependence of the tensile properties of a ferritic stainless steel alloy [8]. This plot shows that as the temperature decreases, the yield strength, σ_o, of the alloy increases faster than its tensile strength, σ_u. For an unnotched, flaw-free specimen, ductility is retained until a very low temperature, where $\sigma_o = \sigma_u$ (point A). This temperature is known as the *nil ductility temperature* (*NDT*); at temperatures lower than the NDT, fracture becomes 100% brittle [1, 2, 8]. One may also see that the presence of a small flaw ($a < 0.1$ in.) raises substantially the NDT of the steel from point A (flaw-free) to point C; for that particular case, the NDT was observed to increase by $\sim$200°F, i.e. 110°C [8]! With materials like bcc metals, the presence of flaws/cracks/notches does not only influence the material's strength, but its toughness as well. The notch sensitivity of a material and the description of available testing methods to estimate it will be discussed in Sect. 2.3.

2.3 Impact Test: Work Principle and Interpretation of Results

The ability of a material to absorb energy in the presence of a sharp notch, often when subjected to impact, is known as *notch toughness* [1]. Materials may be divided into three categories based on their notch toughness [8]:

1. Low- and medium-strength fcc metals and most hcp metals exhibit very high notch toughness; these materials tend to fail invariably in a ductile manner.
2. High-strength materials ($\sigma_o > E/150$) with very low notch toughness; these materials fail in a brittle manner even when the applied stress is in the elastic range. High-strength steels, aluminium, and titanium (Ti; hcp) alloys belong to this category.
3. Low- and medium-strength bcc metals, ceramics, beryllium (Be; hexagonal), and zinc (Zn; hcp) fail in a brittle manner at low temperatures and in a ductile manner at high temperatures. In other words, their notch toughness is temperature dependent. The transition from ductile to brittle fracture for the metals in this category occurs at 0.1–0.2 of their absolute melting temperature, Tm; for ceramics, this transition occurs between 0.5 and 0.7 Tm.

The *notch sensitivity* of a certain material may be evaluated by comparing the absorbed energies of notched and unnotched specimens during impact [2, 9]. Since notches are often present in structural materials (due to poor machining, fabrication, or design), knowing the notch toughness of the materials used in any structure is very useful for the design engineer. Moreover, since the same engineer is interested in the worst possible combination of service conditions that might lead to failure, experimental testing methods were devised that intentionally suppress the ability of the material to deform plastically.

An example of such a test is the *Charpy V-notch impact test*, which (a) imposes high strain rates, and (b) creates a triaxial stress state by introducing a sharp notch to the test specimen. Furthermore, the Charpy V-notch (CVN) impact test can also be performed at low temperatures, limiting even further the ability of the test specimen to deform plastically. Figure 2.12 shows a Charpy impact test set-up, together with various possible test specimen configurations [9]. During testing, a heavy pendulum, starting at an elevation h_0, swings through its arc, strikes, and breaks the specimen, reaching a lower final elevation, h_f. Knowing the initial and final pendulum elevations allows the calculation of the potential energy difference. This difference is mainly the *impact energy* absorbed by the test specimen during fracture. For the Charpy test, this energy is expressed in joules (J) or foot-pounds (ft-lb). The ability of a material to withstand impact is often referred to as *impact toughness*; the impact toughness of a test specimen represents the energy absorbed during its fracture [7]. In this section, the factors affecting the impact toughness of a test specimen will be extensively addressed, so as to ensure (a) the correct evaluation of experimental results and (b) the understanding of the limitations of this testing method.

One could roughly divide the factors affecting impact toughness into (a) factors that are related with the service conditions and (b) factors that are related with the material microstructure. It is important to realise that the factors in these two categories are interlinked in more than one way. Examples of factors in the first category include temperature, loading/strain rate, and degree of material constraint; the response of a certain metal/alloy to these factors is largely determined

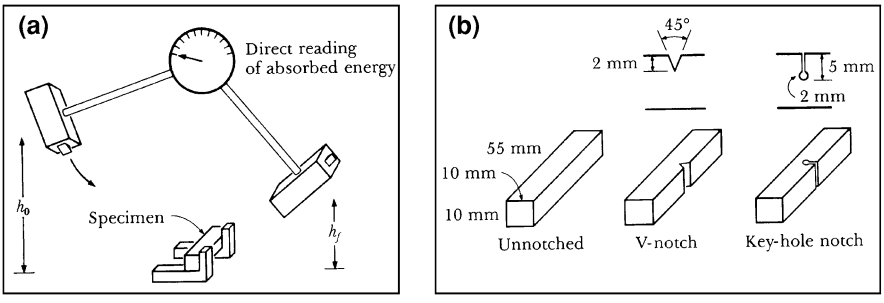

Fig. 2.12 **a** The Charpy impact test set-up [9]#. **b** Typical test specimen configurations designed for Charpy impact testing [9]#

by its crystal structure. For dense (i.e. non-porous) materials, factors belonging to the second category include the alloy composition as well as the volume fraction, size distribution and spacing of brittle second-phase particles, like the IMCs in Pb-free solders. At this point, one could also indicate that the volume fraction, size distribution, and spacing of second-phase particles are dictated by the alloy composition and the processing/service conditions experienced by the alloy. For example, the volume fraction of second-phase particles in an alloy is in principle defined by equilibrium thermodynamics. However, the size distribution and spacing of such precipitates is usually evolving in time, depending on the initial material microstructure (i.e. the microstructure at the end of processing) and the service conditions. The initial microstructure is greatly influenced by the chosen processing conditions, like cooling rate, temperature, and pressure; on the other hand, the service conditions are responsible for the growth and ripening of second-phase particles or the phase transformations that could take place in the material. For porous/cracked materials, the material response to impact is also dictated by the amount, spatial distribution, and orientation of material defects. Figure 2.13a illustrates the influence of the flaw size and flaw orientation on the probability of failure occurrence.

2.3.1 Temperature on Impact Toughness

As mentioned in Sect. 2.2.3, the temperature dependence of the Peierls–Nabarro stress, i.e. the stress required to move a dislocation through a crystal lattice, is more pronounced in bcc metals than in fcc or hcp metals. Since the Peierls–Nabarro stress and the yield strength are interrelated, the yield strength of bcc metals depends on temperature more strongly than the yield strength of fcc or hcp metals. The relative faster increase in the yield strength with respect to the tensile strength upon cooling is the main reason for the low-temperature embrittlement of bcc metals. Figure 2.13b shows the Charpy impact energy of several structural materials as a function of temperature. Some of the materials in this figure exhibit low impact toughness at all temperatures (e.g. the 75-ksi yield strength Al), while others show a high level of impact toughness at all temperatures (e.g. the 180-ksi yield strength steel). As may be seen from the same figure, the impact energy of some materials (Al alloys and high-strength steels) does not change with temperature; these are fcc alloys. On the other hand, the impact energy of some materials (e.g. the 40-ksi yield strength steel) changes dramatically with temperature: these are bcc alloys. Embrittlement occurs around a temperature known as the *ductile-to-brittle transition temperature (DBTT)*.

The exact location of DBTT on the temperature axis and the magnitude of embrittlement are affected by several factors that include the alloy composition, the amount, shape/sharpness, size and spatial distribution of brittle second-phase particles, the loading/strain rate, and the degree of material constraint. Figure 2.14a illustrates the change in the Charpy impact energy of steel as a

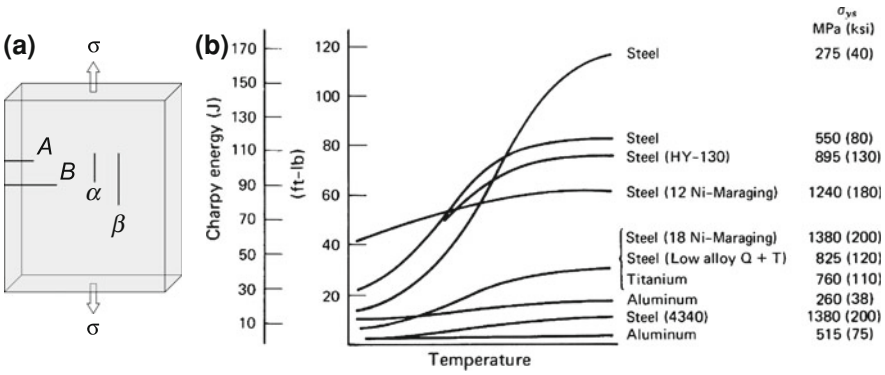

Fig. 2.13 **a** Arbitrary cracks in a solid body subjected to tension; the body contains cracks A, B, α, and β, where $\alpha = A$ and $\beta = B$. Since cracks α and β are parallel to the direction of stress, failure will occur in association with cracks A and B. The fact that $A < B$ increases the probability of failure originating from crack B [2]*. **b** Change of the Charpy impact energy of several engineering alloys with temperature [2] &. & From "Deformation and Fracture Mechanics of Engineering Materials", 4th edition, by Hertzberg. © 1996 by John Wiley and Sons, Inc. Reprinted with permission of John Wiley and Sons, Inc. The meaning of symbol & is the same throughout this text

function of its sulphur (S) content. The observed impact toughness change is attributed to the change in the volume fraction of sulphide inclusions in this steel. Figure 2.14b shows the effect of the shape and sharpness of graphite precipitates on the impact toughness of ferrous alloys: spherical precipitates are quite innocuous, while flake-like precipitates with sharp edges decrease the material's impact toughness. In fact, sharp and brittle second-phase particles, like several IMCs in Pb-free solders, act as *'internal notches'*, reducing the impact toughness of the otherwise ductile metallic matrix in which they have precipitated. These 'internal notches' play the role of stress concentrators inside the matrix material, facilitating the onset of brittle failure. Their impact on material properties is similar to the effect of external notches/cracks on the properties of notch-sensitive materials, like the ductile iron of Fig. 2.14b.

It has been mentioned more than once that the Peierls–Nabarro stress and the yield strength of a certain material are interrelated, and so are their temperature dependences. Since the Peierls–Nabarro stress expresses the resistance of a crystal lattice to dislocation motion, it would be interesting to see how the movement of dislocations is affected by the size and spatial distribution of second-phase particles. In general, second-phase particles in a metallic matrix are obstacles to dislocation motion [2]. After precipitation, the hardness and yield strength of the host alloy increases initially with time, but eventually decreases with prolonged annealing. This trend is demonstrated in Fig. 2.15a, which shows ageing curves of the 6061-T4 aluminium alloy [2]. These curves could be interpreted as follows: after solution treatment and quenching, the alloy is characterised by a maximum potential for solid solution strengthening, since most of the solute is present in the

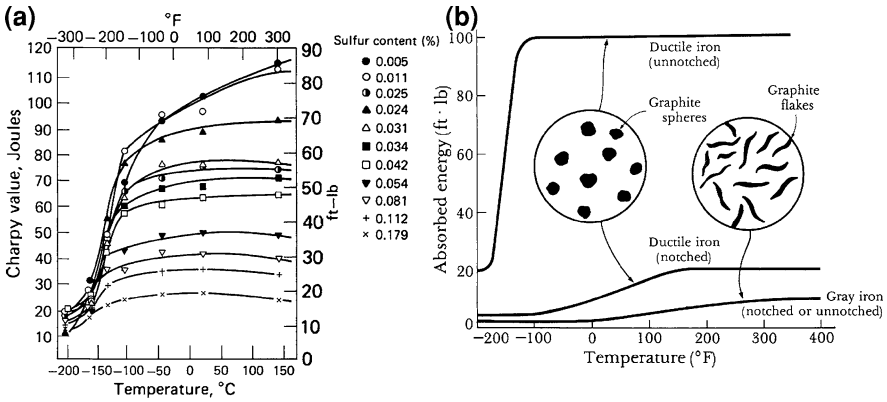

Fig. 2.14 **a** Effect of the *S* content on the Charpy impact energy of a steel plate [2]&. **b** The effect of notches (both external and internal) on the impact properties of two different ferrous alloys. The sharp graphite flakes in the grey iron act as internal notches, resulting in low absorbed energies during impact (i.e. brittle behaviour). On the other hand, the ductile iron contains spherical graphite nodules that do not act as internal notches, thus failing in a ductile manner. However, the presence of external notches reduces substantially the energy absorbed during the fracture of ductile iron [9]#

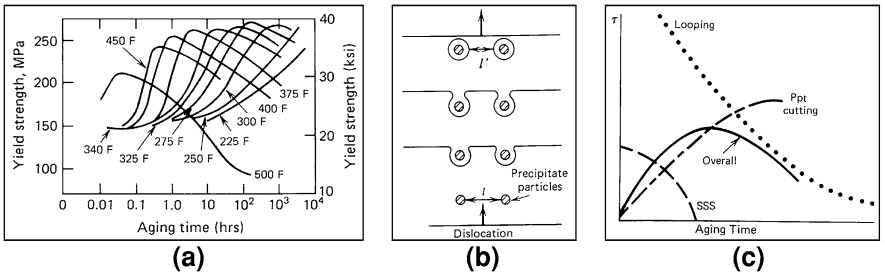

Fig. 2.15 **a** Ageing curves of the 6061-T4 aluminium alloy [2]&. **b** Dislocation looping around second-phase particles [2]&. **c** Schematic representation of the role of the major hardening mechanisms in the overall hardening response of an alloy [2]&. SSS stands for solid solution strengthening, and Ppt stands for precipitate

host lattice. Ageing will lead to the precipitation of second-phase particles, which on the one hand limits the effect of solid solution strengthening but on the other hand results in precipitation hardening (i.e. strengthening) the alloy. Precipitation hardening occurs through several mechanisms, like the interaction of dislocations with misfit strain fields around second-phase particles, particle cutting, and elastic modulus interaction effects. The extent of such hardening increases initially with time and, hence, with the precipitate particle size. Prolonged ageing, however, results in a wider inter-particle spacing, due to the Ostwald ripening

(i.e. coarsening) of the precipitates. When this happens, dislocation looping occurs around the particles (Fig. 2.15b), a fact reflected in the weakening of the alloy, which simultaneously becomes more ductile; this weakening becomes worse with further ageing. The overall response of the alloy to ageing is characterised by maximum strength at intermediate ageing times and second-phase particle sizes (Fig. 2.15c).

The above discussion shows why the presence of IMCs in Pb-free solders alloys has a large impact on their fracture behaviour. Based on what has been said so far, it is expected that mainly IMC particles of a certain (intermediate) size will effectively 'pin' dislocations, limiting thus the capability of the host lattice for plastic deformation. Plastic deformation will be further suppressed with decreasing the temperature, especially for bcc metals, due to the increase in the Peierls–Nabarro stress. An enhanced Peierls–Nabarro stress implies that dislocation motion will occur at a higher stress level, so that the first dislocations to move will do so faster, since their velocity is proportional to the applied stress [8]. Therefore, the presence of IMC particles with the 'right' size and spacing in Pb-free solders stressed at low temperatures will cause dislocation coalescence and crack nucleation in the immediate vicinity of these IMCs, as suggested by Fig. 2.6.

Factors that should be of concern when one strives to control the effect of IMCs on the embrittlement of Pb-free solder alloys include (a) the volume fraction (as defined by the alloy composition), and (b) the shape, size distribution, and spacing of these IMCs (as defined by the microstructure after soldering and the 'mission profile' of the solder joint). In this chapter, these factors will be further discussed only with respect to the IMCs in the bulk solder. The IMC layers forming between solder joint and bond pads will be addressed separately in another chapter of this Handbook.

2.3.2 Strain Rate on Impact Toughness

The loading rates in most structures vary from slow to dynamic; with *slow loading rates*, the maximum load is reached in $\geq$10 s (usually, 10–60 s), while with *dynamic loading*, the maximum load is reached in $\leq$0.001 s [1]. *Intermediate loading rates* vary between the two extremes mentioned above, but typical loading rates in this category require $\sim$1 s to maximum load, as in the case of bridges subjected to truck loadings [1]. The common definition of loading rate is [1]:

$$\dot{K} = \frac{K_{\text{critical}}}{t} \tag{2.4}$$

where $\dot{K}$ = rate of increase in the stress-intensity factor, in MPa$\sqrt{\text{m}}$/s or ksi$\sqrt{\text{in.}}$/s, K_{critical} = critical stress-intensity factor (K_c, K_{Ic}, $K_{Ic}(t)$, K_{Id}), in MPa$\sqrt{\text{m}}$ or ksi$\sqrt{\text{in.}}$, and t = time required to reach K_{critical}, in *s*.

The three loading rate categories are defined as follows [1]:

Slow: $\dot{\varepsilon} \approx 10^{-5}\text{s}^{-1}$
Intermediate: $\dot{\varepsilon} \approx 10^{-3}\text{s}^{-1}$
Dynamic: $\dot{\varepsilon} \approx 10\,\text{s}^{-1}$

where $\dot{\varepsilon}$ is the *strain rate* (i.e. strain per time unit) just ahead of the crack tip in a notched test specimen. Little change occurs in the fracture toughness of a material, unless the loading rate varies by at least one order of magnitude [1]. Figure 2.16a compares the three different loading rates with respect to the available time until failure.

In general, the fracture toughness of structural materials, especially bcc metals, increases with increasing temperature and decreasing loading rate. The first principle is illustrated as a general trend in Fig. 2.16b, while Fig. 2.17a shows fracture toughness data acquired from a 50-ksi yield strength steel [1]. Understanding Figs. 2.16b and 2.17a is easier using the following explanations: as mentioned in Sect. 2.2.1, the *fracture toughness* of a material is given by the *critical stress-intensity factor*, K_c. Specific service conditions, however, produce specific K_c values; an example is the K_{Ic}, which is the *mode I fracture toughness for slow loading under plane-strain conditions* [1]. The *mode I fracture toughness for intermediate loading rates under plane-strain conditions* is referred to as $K_{Ic}(t)$, where the time t to maximum load is given in the parenthesis [1]. Finally, the *mode I fracture toughness for dynamic loading under plane-strain conditions* is referred to as K_{Id} [1]. For a specific material, K_{Ic}, $K_{Ic}(t)$, and K_{Id} are known as the 'static', 'intermediate', and 'dynamic' fracture toughness, respectively, and can be determined as a function of temperature (Figs. 2.16b and 2.17a). Figure 2.16b shows that K_{Ic}, $K_{Ic}(t)$, and K_{Id} increase with the service temperature. However, at any given temperature, the dynamic fracture toughness is lower than both the intermediate and the static fracture toughness [1]; in general, the following relation holds: $K_{Id} < K_{Ic}(t) < K_{Ic}$.

At constant temperature, tests that aim at the determination of fracture toughness and are conducted at higher loading rates typically result in lower fracture toughness values, since $K_{Id} < K_{Ic}(t) < K_{Ic}$ (Fig. 2.17b). The effect of both

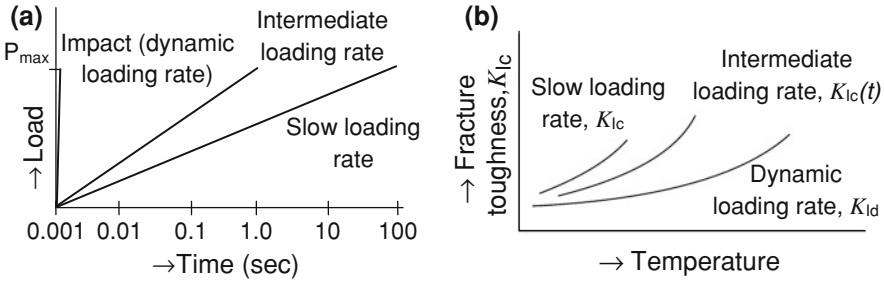

Fig. 2.16 **a** Dependence of the time to failure on the loading rate; P_{max} is the maximum load [1]*. **b** Effect of temperature and loading rate on the fracture toughness [1]*

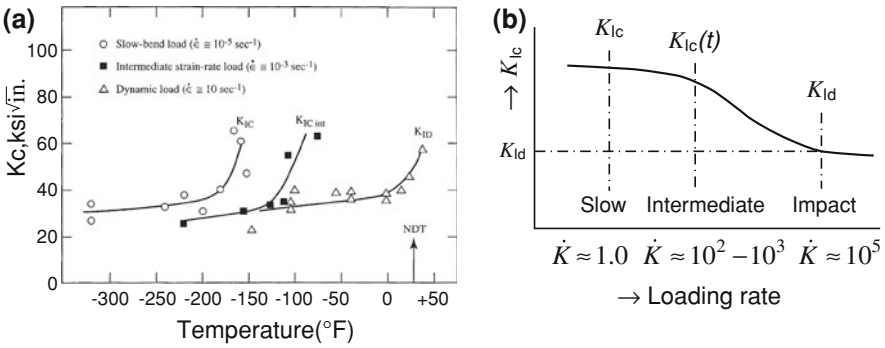

Fig. 2.17 **a** Effect of temperature and strain rate on the fracture toughness of a 50-ksi yield strength steel [1]†. **b** Effect of loading rate, $\dot{K}$, on the fracture toughness at constant temperature [1]*. † From "Fracture and Fatigue Control in Structures: Applications of Fracture Mechanics", 3rd edition, by Barsom and Rolfe. © 1999 by ASTM International. Reprinted with permission of ASTM International. The meaning of symbol † is the same throughout this text

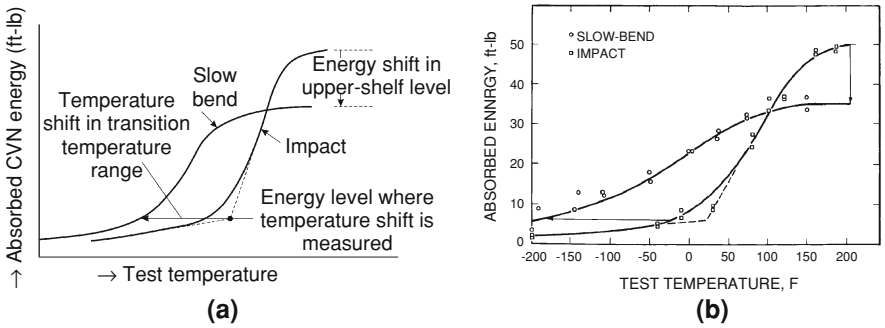

Fig. 2.18 **a** Schematic representation of the shift in the CVN transition temperature and the upper shelf level due to strain rate [1]*. **b** Slow bending and CVN impact test results acquired from an A36 steel [1]†

temperature and loading rate on the fracture behaviour of certain materials is observed in the Charpy V-notch impact test results, as shown schematically in Fig. 2.18a. Experimental results from an A36 structural steel are presented in Fig. 2.18b, which shows that the ductile-to-brittle transition of specimens tested at slow loading rates occurs at lower temperatures in comparison with the transition of specimens tested in impact. It should be pointed out that certain materials, like aluminium alloys, titanium alloys, and high-strength steels (yield strengths $\geq$ 140 ksi), do not exhibit loading-rate effects [1]. The response of these materials to impact may again be related to their crystal structure. For these materials, there would generally be no difference between the K_{Ic} and K_{Id} values that have been measured at the same test temperature [1].

2.3.3 Constraint on Impact Toughness

The concept of *constraint* refers primarily to the transition from a plane-strain to a plane-stress condition, due to changes in the specimen thickness. In linear-elastic fracture mechanics, *plane-strain* is the stress condition, where the strain is zero in a direction normal to both the axis of the applied tensile stress and the direction of crack growth. Plane-strain is related to *maximum constraint* and occurs in very thick specimens with deep cracks. On the other hand, *plane-stress* is the stress condition, where the stress is zero in the thickness direction. Plane-stress is related to *minimum constraint* and occurs in thin test specimens [1, 2]. Figure 2.19 shows schematically the plane-stress and plane-strain conditions. But why would the stress state of the test specimen influence its fracture resistance?

In order to answer this question, one must first understand that a region of plasticity is established near the crack tip of a notched specimen, whenever the stresses ahead of this tip exceed the yield strength of the material [2]. Figure 2.20a illustrates the onset of plastic deformation directly ahead of a crack tip, i.e. at an angle $\theta = 0$. At a certain distance r from the crack tip, the elastic stress will exceed the yield strength, σ_{ys}, of the material, and, at that particular distance, the following relation will hold [1, 2]:

$$\sigma_{ys} = \frac{K_I}{\sqrt{2\pi r}} \tag{2.5}$$

where K_I is the stress-intensity factor. For the plane-stress condition (i.e. biaxial stress state), the radius, r_y, of the plastic zone ahead of the crack tip may be given by the following expression [1, 2]:

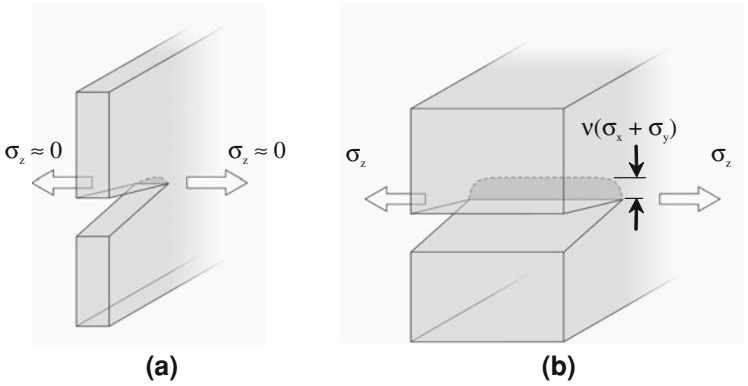

Fig. 2.19 Schematic representation of (**a**) the plane-stress condition for a thin sheet, and (**b**) the plane-strain condition for a thick plate [2]*. In the plane-stress condition, the through-thickness stress, σ_z, is close to zero, i.e. $\sigma_z \approx 0$. In the plane-strain condition, a through-thickness stress develops, which may be given by the expression $\sigma_z \approx \nu(\sigma_x + \sigma_y)$

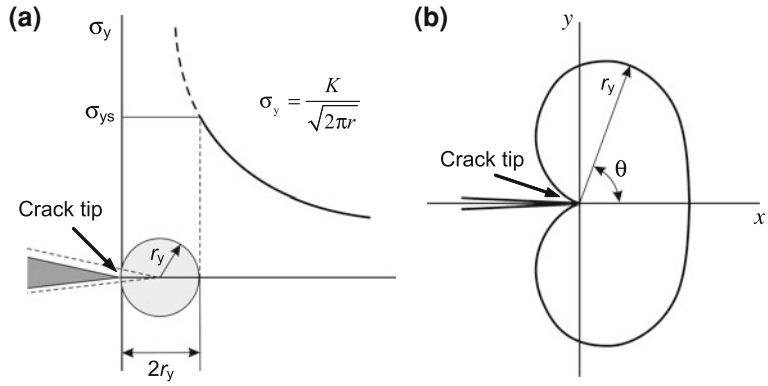

Fig. 2.20 **a** Onset of plastic deformation at the crack tip, where a plastic zone of radius r_y is established [2]*. **b** Boundary of the plastic zone ahead of a crack tip as a function of the angle θ with the horizontal [2]*

$$r_y \approx \frac{1}{2\pi}\frac{K_{IC}^2}{\sigma_{ys}^2} \tag{2.6}$$

For the plane-strain condition, the triaxial stress state ahead of the crack tip reduces the size of the plastic zone. In that case, the radius of the plastic zone is provided by the following expression [1, 2]:

$$r_y \approx \frac{1}{6\pi}\frac{K_{IC}^2}{\sigma_{ys}^2} \tag{2.7}$$

Equations 2.6 and 2.7 show that the size of the plastic zone ahead of a crack tip is smaller in the plane-strain condition than in the plane-stress condition. It must also be noted that the size of the plastic zone ahead of a crack tip varies also with θ, as shown in Fig. 2.20b.

Based on the above, it becomes clear that when the test specimen is thick in the direction parallel to the crack front, a large through-thickness stress, σ_z, will restrict the sample's plastic deformation in that direction. Since the fracture toughness of a material depends on the volume of material capable of plastic deformation prior to fracture and this volume depends on the specimen thickness, the fracture toughness K_c varies with the specimen thickness, as shown in Fig. 2.21a. For a thin sample, the plastic constraint at the crack tip is minimal, and the fracture toughness is, thus, maximum. As the specimen thickness increases, plane-strain conditions are established at the crack tip, increasing the plastic constraint and, thereby, decreasing the fracture toughness. When the specimen thickness exceeds a certain value, the fracture toughness stops decreasing; the lowest fracture toughness value is known as the *plane-strain fracture toughness,* K_{Ic}, and it is the conservative lower limit of material toughness that the design engineer can use for any given application [2]. One could summarise the above by

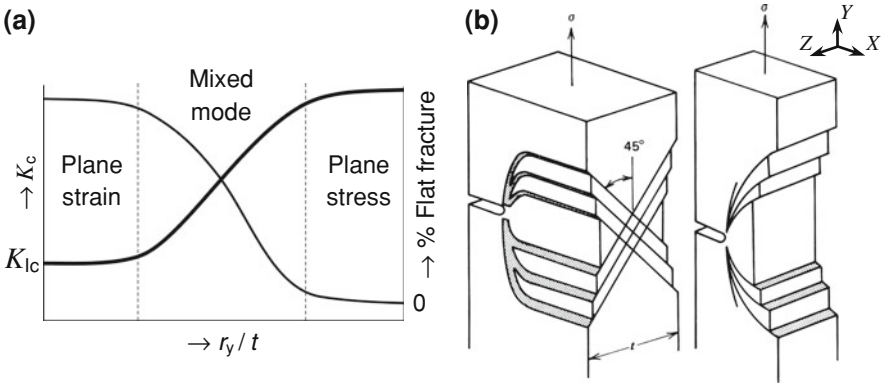

Fig. 2.21 **a** Effect of the plastic zone size-to-plate thickness ratio, r_y/t, on the fracture toughness and macroscopic appearance of the fracture surface. The fracture toughness curve is thicker than that related to the percentage of flat fracture. Plane-stress conditions are associated with maximum fracture toughness and a slant fracture. Plane-strain conditions are associated with minimum fracture toughness and a flat fracture [2]*. **b** Crack-tip deformation patterns in the plane-stress (*left*) and plane-strain (*right*) state [2]&

saying that the plane-stress fracture toughness, K_c, is affected by both metallurgical factors and specimen geometry, while the plane-strain fracture toughness, K_{Ic}, depends only on metallurgical factors [2].

Since the effect of the stress state on the fracture toughness depends on the relation between the size of the plastic zone ahead of a crack tip, r_y, and the specimen thickness, t, it would be interesting to consider the change in the stress state in terms of the ratio r_y/t. Typically, when $r_y/t \geq 1$, plane-stress conditions prevail and the fracture toughness is high. On the other hand, plane-strain conditions exist when $r_y/t < 1/10$. In both cases, the yield strength of the material determines the thickness required for the establishment of plane-stress or plane-strain conditions, since it determines r_y according to Eqs. 2.6 and 2.7. This means that very thin plates of a material with high yield strength can still experience plane-strain conditions, whereas very thick specimens of a low yield strength material may never experience true plane-strain conditions [2].

The dependence of the fracture toughness on the stress state may also result in a transition of the fracture mode from ductile to brittle. As shown in Fig. 2.21a, the relative degree of flat-to-slant fracture depends on the stress state ahead of the crack tip. For plane-stress conditions and $r_y \geq t$, the fracture plane often assumes a $\pm 45°$ orientation with respect to the load axis and sheet thickness (Fig. 2.21b). This happens because failure occurs on the planes containing the maximum resolved shear stress; these planes lie along $\pm 45°$ lines in the *YZ* plane [2]. For plane-strain conditions and $r_y \ll t$, the plane of maximum shear is in the *XY* plane, and the fracture plane lies midway between the two maximum shear planes [2]. The fracture mode transition is observed with materials like aluminium, titanium, and certain steel alloys, as well as with a number of polymers [2]. In general, flat

fracture surfaces imply plane-strain conditions and brittle failures, while slant or shear fracture surfaces are related to plane-stress conditions and more ductile failures [2].

2.3.4 Standard ASTM Fracture Test Methods

Several standard test methods of the American Society for Testing and Materials (ASTM) have been developed to measure the various critical stress-intensity factors for materials with different types of fracture behaviour. Figure 2.22 presents the general regions of the fracture behaviour of structural steels and the ASTM test methods used in each one of them.

The ASTM test methods mentioned in Fig. 2.22 are [1]:

1. K_{Ic}: Plane-strain fracture toughness value obtained at slow loading rates. The material constraint is maximum, leading to unstable brittle fracture with little or no deformation. ASTM test method E-399-90: Standard Test Method for Plane-Strain Fracture Toughness of Metallic Materials.
2. $K_{Ic}(t)$: Plane-strain fracture toughness value obtained at intermediate loading rates, where t is the time to maximum load. The material constraint is maximum, leading to unstable brittle fracture with little or no deformation. ASTM test method E-399—Annex A7: Special Requirements for Rapid-Load Plane-Strain Fracture Toughness $K_{Ic}(t)$ Testing.
3. K_{Ia} (K_{Id} or K_{ID}): Linear-elastic behaviour during dynamic/impact loading that results in fast, unstable brittle fracture. K_{Ia} is the plane-strain crack-arrest toughness, while K_{Id} or K_{ID} is the plane-strain fracture toughness under dynamic loading. K_{Id} and K_{Ia} are assumed to be equivalent, but there is no standard K_{Id} test method. ASTM test method E-1221-96: Standard Test Method

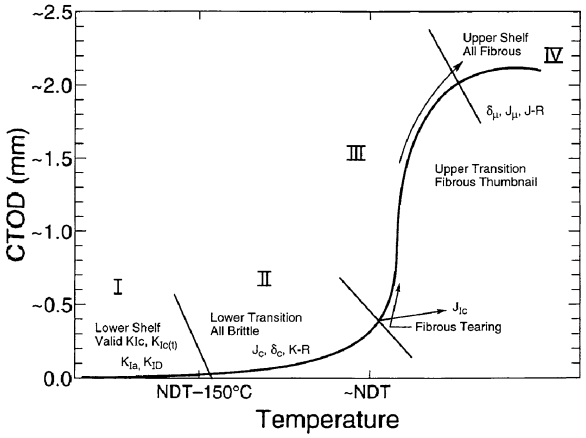

Fig. 2.22 General regions of the fracture behaviour of structural steels [1]†

for Determining Plane-Strain Crack-Arrest Fracture Toughness, K_{Ia}, of Ferritic Steels.

4. δ_c, J_c, *K-R*: Elastic–plastic plane-stress behaviour during slow loading, accompanied by plastic zone development, but without stable crack growth. Fast, unstable brittle fracture occurs.
   δ_c: ASTM Test Method E-1290-93: Standard Test Method for Crack-Tip Opening Displacement (CTOD) Fracture Toughness Measurement.
   K-R: ASTM Test Method E-561-94: Standard Practice for *R*-Curve Determination.
   J_c: ASTM Test Method E-1737-96: Standard Test Method for *J*-Integral Characterisation of Fracture Toughness.
5. J_{Ic}: Critical value of the *J*-integral that describes the stress–strain field ahead of a crack. J_{Ic} is a measure of the fracture toughness at the onset of slow, stable crack growth. The behaviour is non-linear elastic–plastic. ASTM Test Method E-813-89: Standard Test Method for J_{IC}, A Measure of Fracture Toughness.
6. δ_u, J_u, *J-R*: Elastic–plastic behaviour during slow loading, accompanied by slow, stable crack growth. Stable crack growth is either followed by brittle fracture (unstable crack growth) or continues until the separation of the test specimen.
   δ_u: ASTM Test Method E-1290-93: Standard Test Method for Crack-Tip Opening Displacement (CTOD) Fracture Toughness Measurement.
   J_u: This is a point on the *J-R* curve described next, as there is no single standard for J_u.
   J-R: ASTM Test Method E-1152-95: Standard Test Method for Determining *J-R* Curves.
7. J_c, J_{Ic}, *J-R*: New method to cover all *J*-integral test results in one standard. The behaviour is elastic–plastic, with or without stable crack growth. ASTM Test Method E-1737-96: Standard Test Method for *J*-Integral Characterisation of Fracture Toughness.
8. *K*, *J*, CTOD (δ): This standard replaces all previous test methods. A new fracture test method, called the Standard Test Method, has been developed for materials with an unknown type of fracture behaviour. For these materials, the needed type of test method is also unknown prior to testing. A bend or compact test specimen is tested, and the P-Δ_{CMOD} and P-Δ_{LLD} records are analysed either as *K*, *J*, or δ values, depending on the test records. CMOD is the Crack-Mouth Opening Displacement, while LLD is the Load Line Displacement. ASTM Test Method E-1820-96: Standard Test Method for Measurement of Fracture Toughness.
9. K_{Jc}: This test method determines the reference temperature, T_o, which characterises the fracture toughness of ferritic steels. These steels experience the onset of cleavage cracking either at elastic, or elastic–plastic K_{Jc} instabilities, or both. ASTM Test Method E-1921-97: Standard Test Method for the Determination of Reference Temperature, T_o, for Ferritic Steels in the Transition Range.

It falls beyond the scope of this text to explain in detail any of the above test methods. Before closing this section, however, the significance of the four regions in Fig. 2.22 must be briefly explained; these regions are known as the lower shelf (I), the lower transition (II), the upper transition (III), and the upper shelf (IV) region [1]. The behaviour in the *lower shelf region* is brittle, irrespective of the loading rate, and the fracture toughness changes little or not at all with the service temperature. Materials with such behaviour should best be avoided, since their toughness levels do not provide adequate safety margins, except under carefully monitored service conditions. The behaviour is nearly linear-elastic, and K_{Ic} could be used to describe the behaviour of the material in the largest part of this region. The behaviour in the *lower transition region* is elastic–plastic with increasing plastic zone sizes but without stable crack growth (ductile 'thumbnail') prior to the final brittle or mixed-mode fast fracture. Depending on the service conditions, such behaviour is satisfactory for many structural applications. The fracture toughness increases with temperature from approximately the linear-elastic K_{Ic} values to the fracture toughness values at the initiation of a fibrous 'thumbnail' visible to the naked eye. The behaviour in the *upper transition region* is elastic–plastic with large plastic zone sizes and increasing amounts of ductile tearing followed by unstable, mixed-mode fast fracture, but only after considerable deformation. Stable crack growth, i.e. 'thumbnail' behaviour, may occur; in that case, failure starts by stable ductile tearing (recognisable by the presence of a coarse fibrous 'thumbnail' on the fracture surface) and is followed by brittle crack propagation. The behaviour in the *upper shelf region* is generally yielding, and fracture is accompanied by fibrous ductile tearing that occupies the whole fracture surface. The exact point where the upper shelf region begins is ambiguous, due to the large data scatter in the upper transition region. This ambiguity is avoided, if the onset of the upper shelf region is defined at the temperature where fracture becomes 100% fibrous tearing. Figure 2.23 also presents the ductile-to-brittle transition in the fracture behaviour of a material with respect to the four regions discussed above.

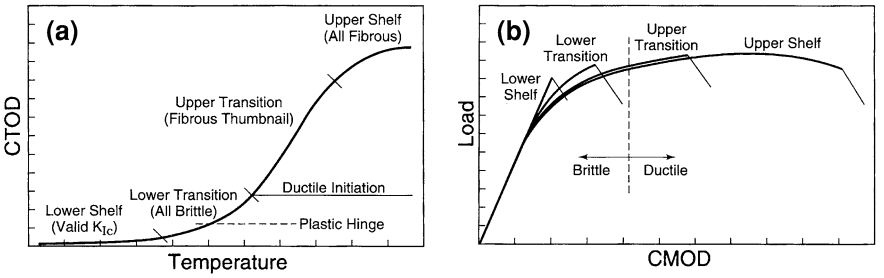

Fig. 2.23 **a** Curve showing the transition in Crack-Tip Opening Displacement (CTOD, i.e. the opening of the notch faces) with temperature [1]†. **b** Load versus Crack-Mouth Opening Displacement (CMOD) curve [1]†

2.3.5 Correlation of K_{Ic} and K_{Id} with CVN Energy

It has often been remarked that one of the main limitations of the CVN impact test is that it only gives a qualitative estimation of the toughness of a material subjected to impact loading, but it is unable to really determine the fracture toughness of the material [4]. In order to address this limitation, a number of methods have been devised [1]; this chapter will present a method to correlate K_{Id} and K_{Ic} with the CVN energy as an example. For the persons interested, additional information on alternative methods may be found in [1].

First, it should be noted that there is an ASTM standard test method dedicated to the impact testing of notched metallic bars. The latest revised version of this standard is the *ASTM Test Method E 23-06: Standard Test Methods for Notched Bar Impact Testing of Metallic Materials* [10]. Second, there seems to be a correlation between the CVN energy measured from the impact testing of a notched metallic material and the impact plane-strain fracture toughness, K_{Id}, of that material [1]:

$$\frac{(K_{Id})^2}{E} = 5(\text{CVN}) \tag{2.8}$$

where E is the material's modulus of elasticity, and K_{Id} is the impact plane-strain fracture toughness, which may be determined using the ASTM test method E-1221-96 (see Sect. 2.3.4). The validity of Eq. 2.8 is illustrated in Fig. 2.24a for various steel grades with yield strength varying in the 36–140 ksi range. The loading rate in all tests was the same, but the notch acuity varied; the latter was taken into account empirically by the factor of 5 [1]. In low-strength steels like

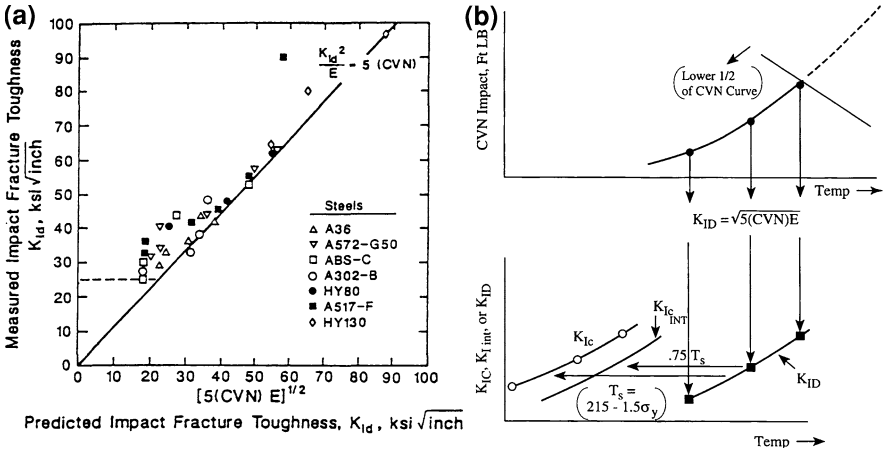

Fig. 2.24 **a** Correlation of the plane-strain impact toughness, K_{Id}, with the CVN energy for various grades of steel [1]†. **b** Relationship between CVN energy, K_{ID}, $K_{Ic}(t)$, and K_{Ic} test results. In these plots, T_s is measured in °F, CVN in ft-lb, K_{ID} in psi$\sqrt{\text{in.}}$, σ_{ys} in ksi, and E in psi [1]†

the ones that produced the data in Fig. 2.24a, a shift in the CVN transition temperature is observed when the loading rate changes from slow bending to impact (see Fig. 2.18a). This shift may be calculated using the following expression [1]:

$$T_{\text{shift}} = 215 - 1.5\sigma_{\text{ys}} \tag{2.9}$$

where σ_{ys} is the 0.2% offset yield strength of the material.

Based on Eqs. 2.8 and 2.9, one may predict the K_{Ic} from CVN impact test results, following the steps of the procedure described below and shown in Fig. 2.24b [1]:

1. Start by testing CVN impact specimens in the lower transition region for the material of interest.
2. At each temperature where CVN values are available, calculate the corresponding K_{Id} values using Eq. 2.8.
3. Shift the K_{Id} values to K_{Ic} values using Eq. 2.9.
4. If fracture toughness values at intermediate loading rates are required, e.g. $K_{\text{Ic}}(t) = K_{\text{Ic}}(1)$ at $t = 1$ s, use ¾ of the K_{Id}-to-K_{Ic} shift, as shown in Fig. 2.24b.

2.3.6 Other Impact Testing Considerations

A problem that often characterises Charpy V-notch impact test results is that the ductile-to-brittle transition of several materials occurs over a whole range of temperatures and not at a specific temperature. In such a case, the definition of the DBTT becomes a challenge. In order to overcome this problem, people have defined the following criteria for the determination of the DBTT [1, 2]:

1. The ductile-to-brittle transition occurs at a certain level of CVN energy, like the 13.5, 20, or 27 J energy level (equivalent to 10, 15, or 20 ft-lb, respectively).
2. The ductile-to-brittle transition occurs at a certain level of lateral expansion on the compression side of the test specimen (Fig. 2.25a).
3. The ductile-to-brittle transition occurs at a certain amount of fibrous (i.e. ductile) or cleavage (i.e. brittle) fracture as measured on the fracture surface of the test specimen (Fig. 2.25b).

The problem with having more than one criterion does not only lie in which criterion to choose. Unfortunately, transition temperatures defined using the energy absorption, ductility, or fracture surface appearance criteria do not agree for the same material! An example is given in Table 2.1, which shows that the transition temperatures of different steels defined by the 20-J energy criterion and the 0.38-mm (15-mil) lateral expansion criterion are in reasonable agreement, but they are both lower than the transition temperature defined by the 50% fibrous fracture criterion.

In contrast to the results presented in Table 2.1, Fig. 2.26 presents CVN test results from a low-strength steel, showing that the transition temperatures defined

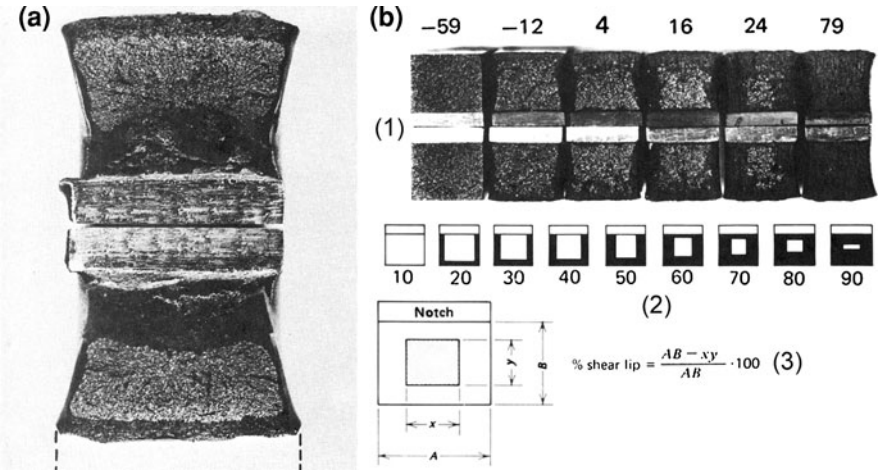

Fig. 2.25 **a** Measurement of lateral expansion at the compression side of a Charpy bar [2]&. **b** Transition in the appearance of the fracture surface of A36 steel Charpy bars as a function of temperature. This figure shows (1) an actual fracture series of A36 steel test specimens, (2) a standard comparison chart showing the percentage shear lip, and (3) the formula used for the calculation of the percentage shear lip [2]&

Table 2.1 Transition temperature data from selected steels [2]

Material	$\frac{\sigma_{ys}}{\sigma_{ts}}\left(\frac{\text{MPa}}{\text{MPa}}\right)$	DBTT (°C)		
		20 J	0.38 mm	50% fibrous
Hot-rolled C–Mn steel	$\frac{210}{442}$	27	17	46
Hot-rolled, low-alloy steel	$\frac{385}{570}$	−24	−22	12
Quenched and tempered steel	$\frac{618}{688}$	−71	−67	−54

σ_{ys} is the yield strength of the material, σ_{ts} is its tensile strength

by the 15 ft-lb energy, 20-mil lateral expansion, and 50% fracture appearance criteria coincide at ∼30°F. This indicates that the right choice of criterion plays an important role in getting reasonable results, but this choice is rarely known a priori. It should also be emphasised that the transition temperature value will also be influenced by other factors, like the specimen size and shape, and the sharpness of the notch [2], so one needs to be very cautious when interpreting impact test results.

One of the factors that merits more consideration is the specimen size, and, in particular, the specimen thickness. As mentioned in Sect. 2.3.3, changes in the specimen thickness affect the degree of material constraint and can be responsible for a transition in the stress state from plane-stress (thin specimens) to plane-strain (thick specimens) conditions. It is already clear that the determined fracture toughness in each one of these conditions is different, with the plane-strain fracture

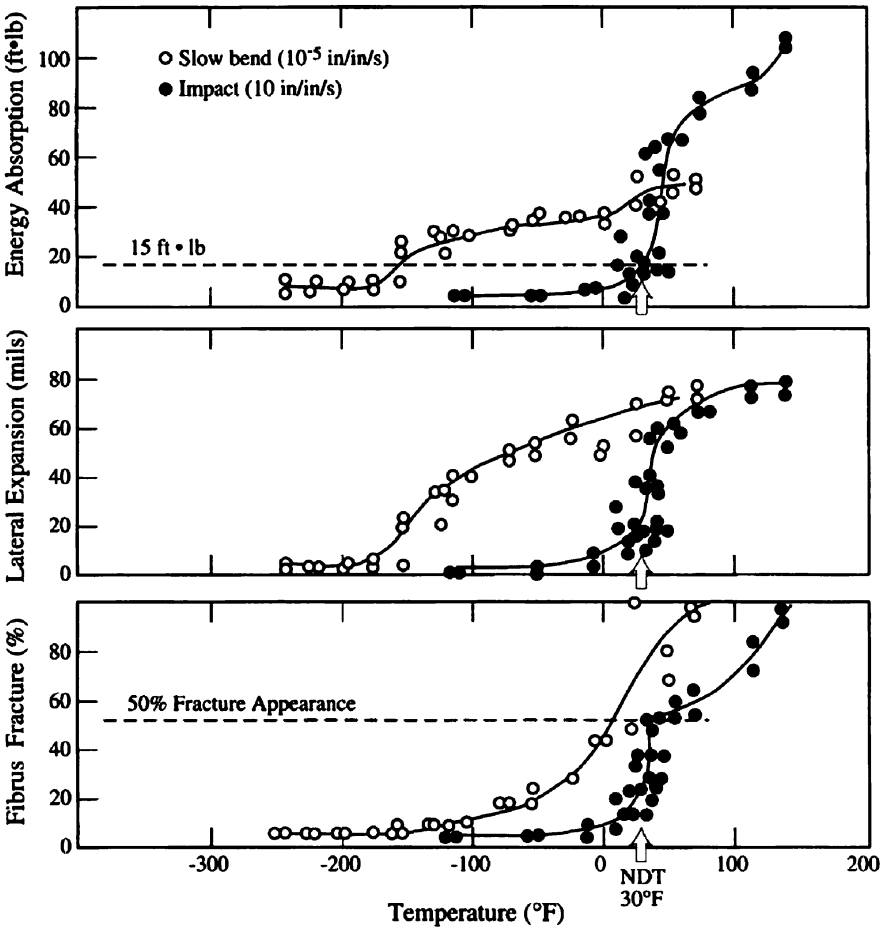

Fig. 2.26 CVN energy absorption, lateral expansion, and fibrous fracture from the impact and slow-bend testing of standard CVN specimens of a low-strength structural steel [1]†

toughness being lower than the plane-stress one (Fig. 2.21a). What may not be clear, however, is that the experimentally determined DBTT often depends on the thickness of the test specimen [2]. This phenomenon is also related to the transition from plane-stress to plane-strain conditions, which is likely to occur as the text specimen dimensions change. For example, Fig. 2.27 shows that the ductile-to-brittle transition temperature of A283 steels increases with the thickness of the Charpy test specimens [2]. This figure shows that the absorbed energy per 2.5 mm of sample thickness, or the percentage of shear fracture, changes at a certain temperature, indicating the transition in the fracture behaviour of these steels from ductile to brittle. As the specimen thickness increases, the DBTT is observed to increase until a limiting value, which most likely corresponds to true plane-strain conditions in the material. Studies like the above point out that one needs to keep in mind the

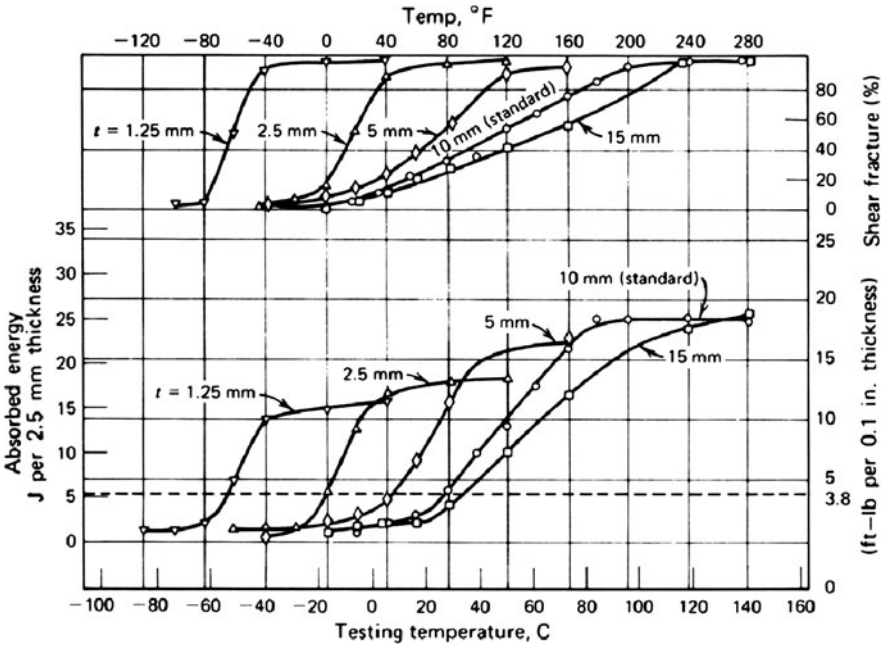

Fig. 2.27 Adjusted energy vs. temperature and shear fracture vs. temperature curves for 38-mm-thick plates of A283 hot-rolled carbon manganese steel tested in impact using CVN specimens of various thicknesses. The DBTT is defined at an absorbed energy level of 5.2 J per 2.5 mm (3.8 ft-lb/0.1 in.) of specimen thickness [2]&

potential DBTT dependence on the specimen thickness when interpreting the impact test results of certain materials. For all the reasons explained in this chapter, the Sn-based Pb-free solder alloys, for example, are expected to exhibit a similar dependence of their DBTT on the test specimen dimensions.

2.4 Fracture Behaviour of Sn-Based Pb-Free Solders

This section reports and discusses experimental results related to the fracture behaviour of commercial Sn-based Pb-free solder alloys, focusing on the conditions under which bulk embrittlement is promoted. The section starts by presenting results acquired from the impact testing of specimens with different geometries and with one of the following compositions (all in wt%): SAC 305 (Sn-3%Ag-0.5%Cu), SAC 405 (Sn-4%Ag-0.5%Cu), Sn-5%Ag, Sn-0.7%Cu-0.1%Ni, Sn-0.7%Cu, 99.99% Sn, and, for the sake of comparison, Sn-37%Pb (near-eutectic Sn–Pb alloy). Apart from the energy absorbed during impact testing, a fractography study of selected samples tested in impact is presented; this study was conducted using scanning electron microscopy (SEM). In order to investigate the

effect of IMC particle size changes on the fracture behaviour of Sn-based Pb-free solders, SAC 405 specimens were subjected to post-casting annealing in the 150–175°C range prior to impact testing; the results of this study are also presented here. Furthermore, SEM was utilised to study the interaction of cracks and IMC particles in solders SAC 405 and Sn-0.7%Cu-0.1%Ni; the cracks formed and propagated during routine thermal cycling of these solders. Finally, this section presents the results of a study of the embrittlement of Sn-based solders due to the formation of "tin pest"; for this purpose, Sn-0.5%Cu ingots were aged at −18°C for a period of up to 2 years.

2.4.1 Ductile-to-Brittle Transition

2.4.1.1 CVN Impact Testing of Bulk Solder Samples

As already mentioned in the introduction of this section, bulk specimens of various commercial Sn-based Pb-free solders and of the Sn-37%Pb solder were tested according to the CVN impact test methodology described in ASTM standard E 23-06 [10]. Standard specimens of $10 \times 10 \times 55$ mm^3 were made from alloys SAC 305, SAC 405, Sn-5%Ag, and Sn-37%Pb, while smaller specimens of $5 \times 5 \times 55$ mm^3 were made from alloys Sn-0.7%Cu-0.1%Ni, Sn-0.7%Cu, and 99.99% Sn, due to the limited availability of the last three alloys [11, 12]. The experimental procedure is described in [11, 12], and the impact test results are discussed later in this section. Due to the two different test specimen dimensions, the impact test results are presented in two plots, following the guidelines of the ASTM standard E 23-06 [10], which recommends the separate presentation of impact results obtained from specimens of different size or shape.

Before commenting on the results obtained from the CVN impact testing of the aforementioned Sn-based Pb-free solders, it is worthwhile mentioning that Sn has the *body-centred tetragonal (bct)* crystal structure [13]. This Sn form, also known as *β-Sn*, transforms at 13.2°C to *α-Sn*, which has the *diamond cubic* crystal structure. The transformation of *β*-Sn-to-*α*-Sn (i.e. the notorious *"tin pest"*) is very sluggish, requiring a large incubation period (about 18 months) below 13.2°C. Therefore, even at low service temperatures, *β*-Sn is the crystalline form of reference for all Sn-based Pb-free solders. It should be pointed out that the bct crystal structure resembles greatly the bcc structure in terms of crystal symmetry and directionality of bonding forces, as illustrated in Fig. 2.28. This means that some of the properties of pure Sn and Sn-based alloys are expected to be comparable to the respective properties of bcc metals: one of them is the existence of a rather sharp transition from ductile to brittle failure at a given DBTT.

In agreement with this expectation, Figs. 2.29 and 2.30 show that the tested Sn-based Pb-free solders demonstrate a sharp ductile-to-brittle transition in the −20 to −130°C range. In contrast to the Sn-based solders, the near-eutectic Sn–Pb solder shows a very gradual and rather weak transition between 0 and −80°C. This

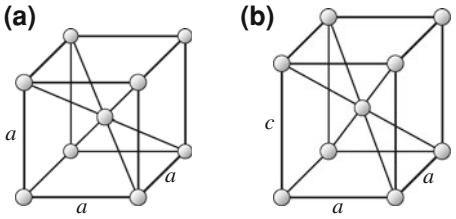

Fig. 2.28 Schematic representation of (**a**) the body-centred cubic (bcc) crystal structure, and (**b**) the body-centred tetragonal (bct) crystal structure

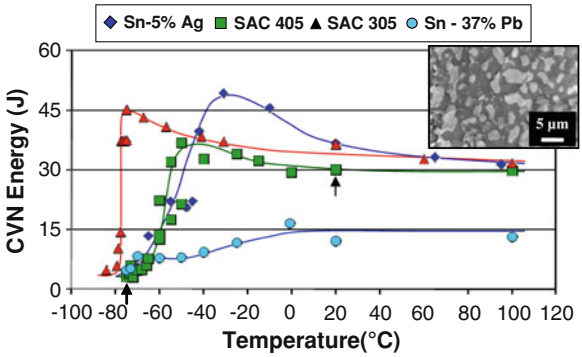

Fig. 2.29 Change of the CVN energy of Sn-37%Pb and various Sn-based solders as a function of temperature [11, 12]*. The specimen dimensions were 10 × 10 × 55 mm^3. The notch depth was 2.5 mm. The inset shows the microstructure of the Sn-37%Pb solder, where the Pb-rich phase appears bright and the Sn-rich phase grey. Data from imec

gradual and not-so-sharp overall transition in fracture behaviour is easy to understand, taking into account that the microstructure of the near-eutectic 63%Sn-37%Pb alloy consists of dendritic grains of a Pb-rich solid solution in a matrix of Sn [14]. The fracture behaviour of a 'composite' material like the Sn-37%Pb solder is expected to be a compromise between the fracture behaviours of its constituents, i.e. the Sn-rich solid solution (bct) and the Pb-rich solid solution (fcc). The fact that bcc and bct alloys tend to exhibit a ductile-to-brittle transition, while fcc alloys do not, explains the fracture behaviour of the Sn-37%Pb solder demonstrated in Fig. 2.29. The microstructure of the Sn-37%Pb solder is also shown in Fig. 2.29. Other comments that could be made on the test results of Figs. 2.29 and 2.30 are:

1. The DBTT of the Ag-containing alloys increases with the Ag content (Fig. 2.29). This is presumably related to the increase in the volume fraction of Ag_3Sn IMCs in the solder. These IMCs are believed to act as internal 'notches' with high stress intensity in their immediate vicinity, facilitating locally the solder embrittlement and shifting the DBTT towards higher temperatures.

2. The nearly pure Sn solders (i.e. Sn-0.7%Cu-0.1%Ni, Sn-0.7%Cu, and 99.99% Sn) exhibit a substantially lower DBTT in comparison with the two SAC solder alloys and the Sn-5%Ag one. To be precise, the DBTT of the very Sn-rich solders is around −130°C, while the lowest DBTT of the Sn-Ag-(Cu) solders is around −80°C (for the SAC 305). This could be attributed to a number of reasons: first, the very Sn-rich solders have a very limited amount of IMCs. Second, the very Sn-rich test specimens were smaller ($5 \times 5 \times 55$ mm^3) than the Sn-Ag-(Cu) test specimens ($10 \times 10 \times 55$ mm^3). This means that the stress state in the smaller specimens might be closer to plane-stress than to plane-strain. As has already been said, the plane-strain toughness is lower than the plane-stress one, which implies that the initiation of brittle failure is easier for plane-strain than for plane-stress conditions. This is reflected in the increase in the DBTT with the specimen thickness, as shown in Fig. 2.27.
3. The notch size in the nearly pure Sn impact test specimens was not the same: for the Sn-0.7%Cu alloy, the notch was 1.3 mm, while for the other two alloys, the notch was 2.5 mm. Interestingly, one may notice that the energy absorbed during the impact failure of Sn-0.7%Cu specimens was higher than the energy absorbed by the other two very Sn-rich alloys (Fig. 2.30). This confirms the notch sensitivity of Sn-based alloys, pointing out that the effective control of the bulk embrittlement of Sn-based solders requires control over the presence of notches in these materials. This automatically implies control over the shape, sharpness, size distribution, and spacing of the IMC particles, which act as 'internal notches'.

Figures 2.31 and 2.32 show SEM micrographs of the fracture surface of selected specimens that have been tested in impact. The chosen specimens, made of the SAC 405 and 99.99% Sn solders, are indicated in Figs. 2.29 and 2.30 with arrows. As may be seen from Figs. 2.31 and 2.32, the fracture behaviour of both the 99.99% Sn and the SAC 405 solders changes drastically as the test temperature decreases. For example, the fracture of the 99.99% Sn solder at room temperature appears to be completely ductile, and the study of its fracture surface reveals boundaries of Sn grains that have been clearly 'stretched' during

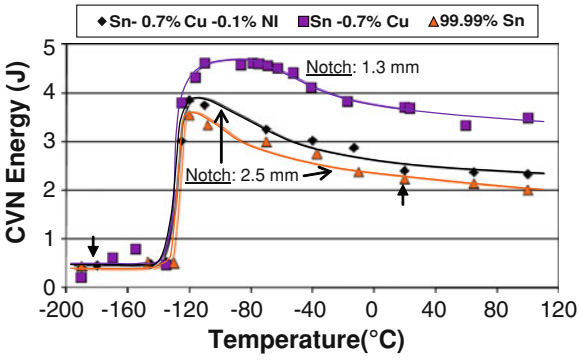

Fig. 2.30 Change of the CVN energy of various Sn-based solder alloys as a function of temperature [11, 12]*. The specimen dimensions were $5 \times 5 \times 55$ mm^3. The notch depth was either 1.3 mm or 2.5 mm. Data from imec

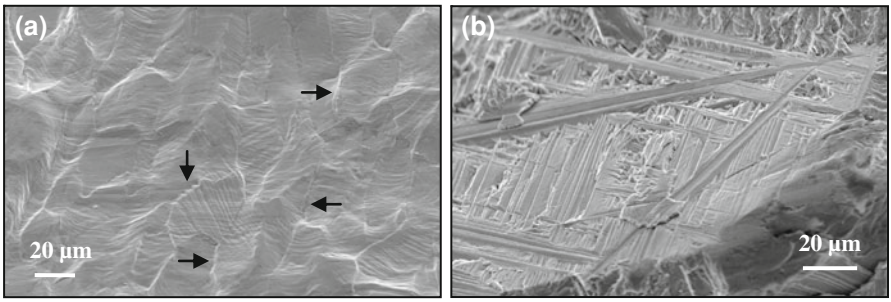

Fig. 2.31 Secondary electron (SE) detector images of the fracture surfaces of impact test specimens made of the 99.99% Sn solder. **a** Specimen tested at room temperature. The *arrows* indicate Sn grain boundaries. **b** Specimen tested at −190°C. Data from imec

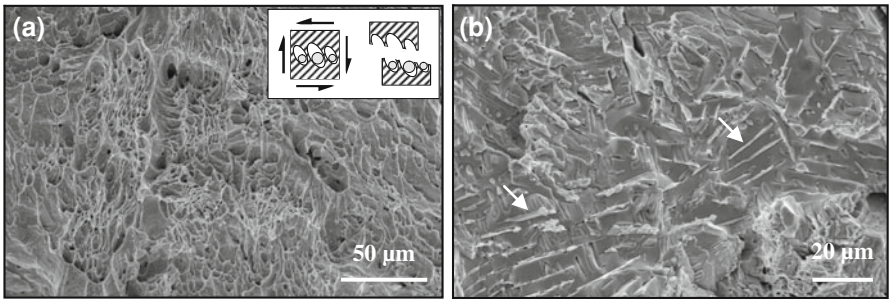

Fig. 2.32 SE detector images of the fracture surfaces of impact test specimens made of the SAC 405 solder. **a** Specimen tested at room temperature. The fracture surface is characterised by the presence of many 'dimples'. The idealised drawing in the inset shows two stages in the dimple-formation process; the dimples form around the hard, brittle IMCs in the soft, ductile Sn matrix and are slightly elongated since the material is sheared during the CVN impact test. **b** Specimen tested at −75°C. The flat grey areas are Sn, while the bright particles indicated by *arrows* are IMCs. Data from imec

testing (Fig. 2.31a). The same solder fails in a completely brittle manner at −190°C, and the study of its fracture surface reveals the cleavage-like fracture of Sn (Fig. 2.31b).

The thorough fractography study of the commercial Sn-based solders mentioned in this text has revealed great similarities between their fracture behaviour and that of nearly pure Sn (i.e. 99.99% Sn). This was not unexpected, as the above solders consist of a dispersion of IMC particles in a matrix of Sn. For example, the fracture surface of a SAC 405 specimen tested in impact at room temperature is typical for the failure of a soft, ductile material containing hard, brittle second-phase particles (Fig. 2.32a). In such a case, failure is believed to occur by microvoid coalescence, and the resulting fracture surface contains numerous depressions, known as 'dimples'. The dimples are created during the stressing of the solder material, which leads to decohesion of the IMC particles from the Sn

matrix and the formation of microvoids around them (inset of Fig. 2.32a); the coalescence of these microvoids leads to the formation of cracks and, eventually, to the failure of the material [2]. The fracture behaviour of SAC 405 is clearly brittle when the material is tested at −75°C, as shown in Fig. 2.32b; the solder embrittlement is mainly the outcome of the low-temperature embrittlement (under conditions of dynamic loading and in the presence of IMC 'internal notches') of the bct Sn matrix.

2.4.1.2 Impact Testing of Solder Joints

This section discusses the results of the fractography study performed on Sn-based solder joints tested in impact. The test specimens consisted of bumped SuperB-GA® packages mounted on FR-4 circuit boards; for this purpose, solder spheres of 750 μm in diameter made of various Sn-based solder alloys were soldered onto Cu bond pads. The specimens were tested in impact using a miniaturised Charpy test set-up built at imec; this customised set-up and the impact test results are presented elsewhere [15, 16]. Figure 2.33 shows SEM images of a SAC 405 solder joint that was tested in impact at room temperature. The fracture of this joint was clearly ductile as it was preceded by appreciable plastic deformation and necking (Fig. 2.33a), while the fracture surface revealed the presence of dimples caused by the IMC particles in the Sn matrix (Fig. 2.33b).

The study of the solder joint surface (indicated by arrows in Fig. 2.33a), which was subjected to tension during impact testing, proved also to be quite interesting, as it revealed the multiple brittle fractures of close-to-the-surface Cu_6Sn_5 IMC particles (Fig. 2.34). These IMCs, being brittle in nature and, hence, prone to failure when subjected to tension, have been forced to break at several sites along their length, so as to follow the deformation of the ductile Sn matrix in which they were embedded. The sharp external notches created in the solder joint by such IMC failures might facilitate the in-service brittle failure of the joint, especially

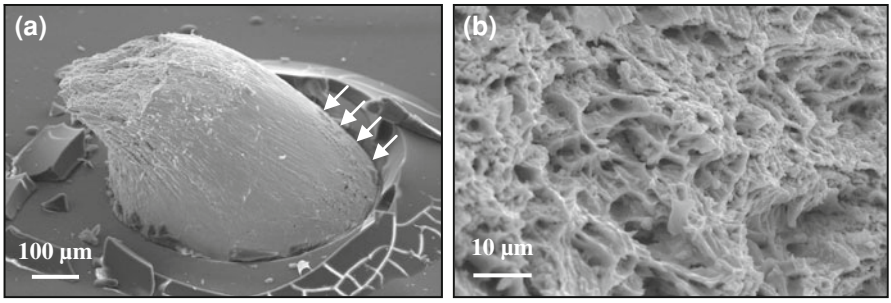

Fig. 2.33 SE detector images of a SAC 405 solder joint that was tested in impact at room temperature. **a** The solder joint failed in a ductile manner, showing appreciable plastic deformation and necking. **b** The fracture surface of the solder joint is characterised by numerous dimples related to the presence of IMCs in the solder. Data from imec

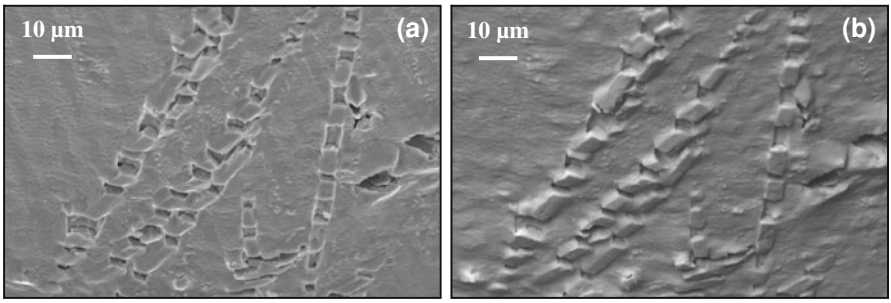

Fig. 2.34 Additional SEM micrographs of the SAC 405 solder joint shown in Fig. 2.33. **a** SE detector image of the area on the solder joint surface, which is indicated by arrows in Fig. 2.33a. This area, which has been subjected to tension during the impact testing of the joint, contains several fragmented Cu_6Sn_5 IMC particles. **b** Backscattered electron (BSE) detector image of the area shown in Fig. 2.34b. Data from imec

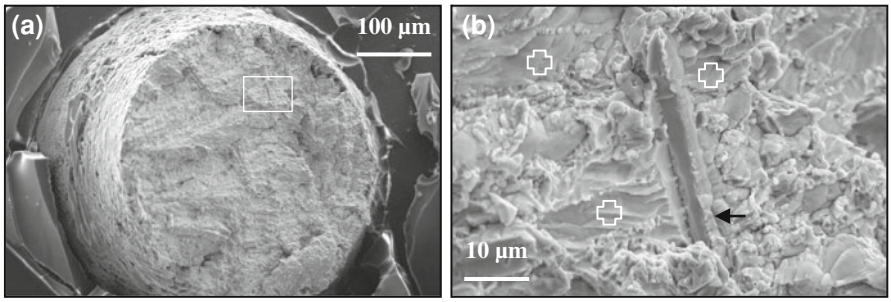

Fig. 2.35 SE detector images of a SAC 305 solder joint that was tested in impact at −70°C. **a** The fracture of the solder joint was clearly brittle, as indicated by the absence of plastic deformation. **b** Closer view of the area outlined by the small *frame* in Fig. 2.35a: the flat areas marked by *crosses* were nearly pure Sn, a fact that demonstrates the bulk embrittlement of the Sn-based solder at −70°C. The precipitate indicated by the *arrow* is a Cu_6Sn_5 IMC particle. Data from imec

when the 'mission profile' of the joint foresees combinations of shocks/intense vibrations with thermal excursions to low temperatures. The fracture behaviour of SAC 305 and other Sn-based commercial solders at room temperature was comparable to that of SAC 405, i.e. failure in the bulk of the joint occurred in a ductile manner [15, 16].

Figure 2.35 shows SEM images of the fracture surface of a SAC 305 solder joint that was tested in impact at −70°C. As may be seen, the joint failed in a brittle manner, i.e. failure was not preceded by plastic deformation, and the resulting fracture surface was macroscopically flat (Fig. 2.35a). On the microscopic level, the fracture behaviour of the nearly pure Sn solder matrix was also

brittle, exhibiting a very flat fracture surface (Fig. 2.35b). The fracture behaviour of SAC 405 and the other Sn-based solders was similar to that of SAC 305 at low temperatures, i.e. brittle [15, 16]. In general, it was observed that the IMC particles in the tested Sn-based solders failed in a brittle manner over the whole test temperature range, i.e. between room temperature and −107°C, while the fracture of the Sn-rich solder matrix changed progressively from ductile to brittle as the test temperature decreased.

2.4.2 Microstructural Aspects of the Ductile-to-Brittle Transition

2.4.2.1 IMC Size Distribution and Spacing on DBTT

As discussed in Sect. 2.3.1, controlling the fracture behaviour of Pb-free solders requires the control of the shape, size distribution, and spacing of the IMCs. The results of an attempt to do just that are shown in Fig. 2.36, which presents the microstructural evolution of a SAC 405 solder caused by post-processing annealing. This alloy has been cast in a small mould, in order to produce a fine dispersion of Ag_3Sn IMCs in the as-cast bulk solder (Fig. 2.36a). Specimens of that casting were annealed for 100 and 1,000 h at 150°C (Fig. 2.36b and c, respectively), and 1,000 h at 175°C (Fig. 2.36d). The comparison of the micrographs in Fig. 2.36 reveals that the size and spacing of the Ag_3Sn IMC particles increases with the temperature and duration of annealing. On the other hand, the sharpness of these IMCs (as expressed by the radius of curvature of the particle edges) decreases with the intensification of the post-casting annealing. As-cast and annealed specimens were tested using a standard CVN impact test set-up, and the change in the DBTT of the alloy was related to changes in its microstructure [17]. Table 2.2 gives an overview of the change in the DBTT with the annealing conditions.

As may be seen for the results of this study, the DBTT decreases as both the temperature and the duration of the post-casting annealing increase. This may surely be related to the change in the size, sharpness, and spatial distribution of the IMC particles in the SAC 405 solder. It is thought that the finer IMCs in the as-cast solder pin the dislocations more effectively than the coarser ones after annealing. Dislocation pinning restricts the capability of the alloy for plastic deformation, facilitating embrittlement. Moreover, the sharper the IMC particles, the higher the intensity of stress concentration in their neighbourhood; making these particles more round is one way to lower the probability that brittle in-service failure will be triggered by their presence in the solder bulk.

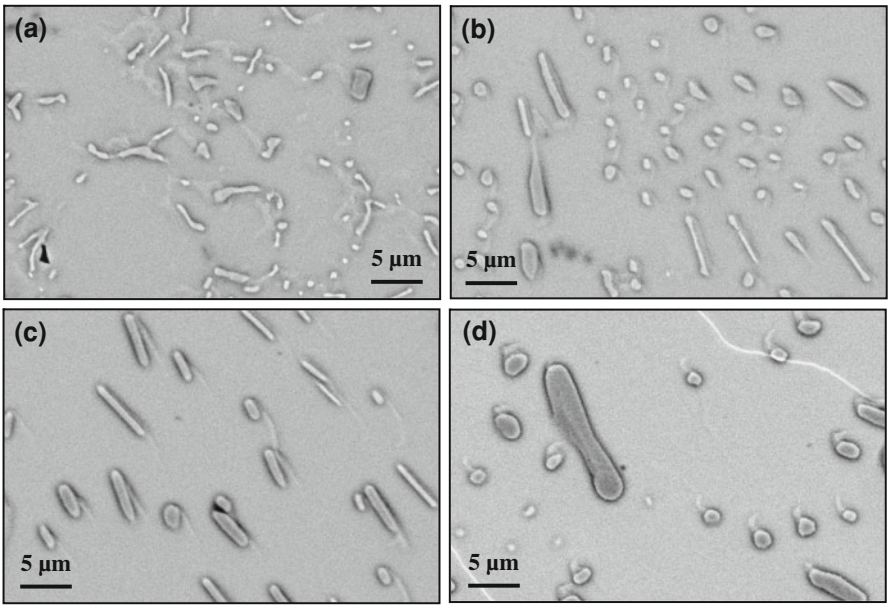

Fig. 2.36 BSE images of the changes in the microstructure of a SAC 405 solder alloy with the temperature and duration of post-processing annealing [17]. The alloy is studied in **a** the as-cast condition, **b** after 100 h at 150°C, **c** after 1,000 h at 150°C, and **d** after 1,000 h at 175°C. Data from imec

Table 2.2 DBTT of SAC 405 versus post-casting annealing conditions [17]

Material condition	DBTT (°C)
As-cast	−28 ± 6
100 h at 150°C	−42 ± 5
1,000 h at 150°C	−40 ± 5
1,000 h at 175°C	−48 ± 5

2.4.2.2 IMC Interaction with Crack Path During Thermal Cycling

Figure 2.37 shows SEM images of a SAC 405 solder alloy that has failed after 175 cycles of thermal cycling between 0 and 100°C. The images of Fig. 2.37 provide evidence of crack nucleation at IMC particles in the bulk of the solder joint. As already mentioned, sharp precipitates like the IMCs in Fig. 2.37 may be considered as internal 'notches' in Pb-free solders. Since Sn-based solders, like the SAC 405 studied here, are notch sensitive (see Fig. 2.30), one must be aware of the effect of the presence, sharpness, and size distribution of IMCs on the bulk embrittlement of such Pb-free solders.

At this stage of the research, it is thought that IMCs, like the Ag_3Sn particle in Fig. 2.37b, tend to pin dislocations, which in turn coalesce and result in crack

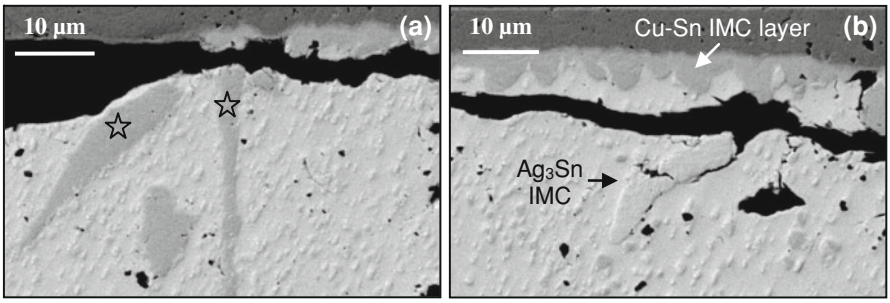

Fig. 2.37 BSE images of cross-sections through a solder joint made of SAC 405 that failed after 175 cycles of thermal cycling between 0 and 100°C. **a** Sharp Cu-Sn IMC particles *(stars)* act as sites of crack nucleation close to the joint surface. **b** Sharp Ag_3Sn IMC particle acts as site of crack nucleation far away from the joint surface. Data from imec

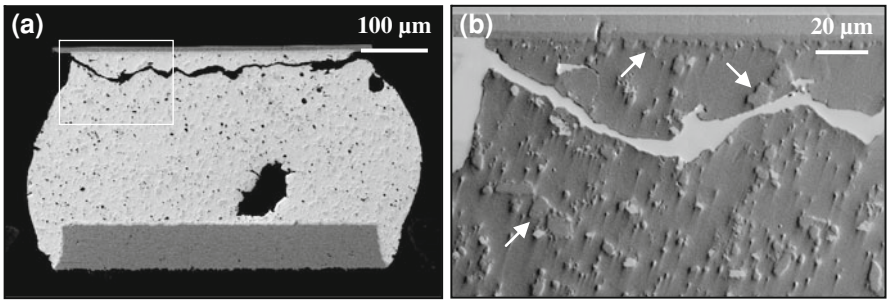

Fig. 2.38 BSE images of a cross-section through a Sn-0.7%Cu-0.1%Ni solder joint that failed after 434 cycles of thermal cycling between −40°C and 125°C. **a** Overview of the solder joint, which has failed due to the propagation of a fatigue type of crack. **b** Detail of the area inside the white *frame* in Fig. 2.38a. The *arrows* indicate IMC particles, which have mainly the $(Ni, Cu)_3Sn_4$ composition. Data from imec

nucleation. Once nucleated, the cracks may propagate either in a catastrophic (i.e. brittle) way through the Pb-free solder joint or in a more energy-absorbing (i.e. ductile) manner, like in the case of the thermo-mechanical fatigue cracks shown in Figs. 2.38 and 2.39. The way the crack will propagate through the solder joint will primarily depend on the service conditions, i.e. temperature, strain rate, and degree of material constraint for a specific structural application. Figures 2.38 and 2.39 show the propagation of fatigue-like cracks in two different joints made of the Sn-0.7%Cu-0.1%Ni solder. These solder joints belonged to BGAs subjected to thermal cycling between −40 and 125°C. The solder joint in Fig. 2.38 is a corner bump, while the joint in Fig. 2.39 is the bump next to the corner one in the array. Due to the fact that the corner bumps suffer the most during thermal cycling, the solder joint in Fig. 2.38 has failed completely, while the degree of damage in the joint of Fig. 2.39 is smaller. Since the corner joints are situated furthest away

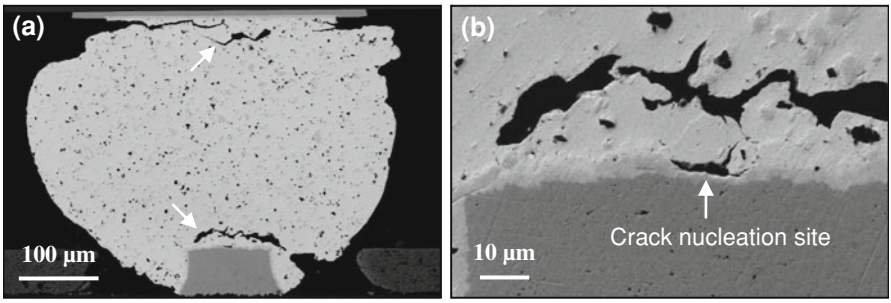

Fig. 2.39 BSE images of a cross-section through a Sn-0.7%Cu-0.1%Ni solder joint that failed after 577 cycles of thermal cycling between −40°C and 125°C. **a** Overview of the solder joint: fatigue-like cracks (indicated by *arrows*) propagate close to both upper and lower bond pads. **b** Crack nucleation between the solder bulk and the interfacial IMC layer. Data from imec

from the neutral point of the whole array, they are subjected to very high thermal stresses during thermal cycling. Thermal stresses are created due to the thermal expansion coefficient mismatch between the joint and its immediate surroundings, e.g. bond pad and PCB.

At this point, one may argue that the failure of the solder joints in Figs. 2.38 and 2.39 is thermo-mechanical fatigue and, as such, it falls outside the scope of this chapter. This is partly true, because the zigzagging of the cracks responsible for the failure of the two Sn-0.7%Cu-0.1%Ni joints suggest an energy-absorbing, rather ductile failure. However, a closer inspection of the sites of crack nucleation reveals that they are mostly related to the IMCs in the solder bulk or the IMC layers formed at the joint/bond pad interfaces. As emphasised throughout the development of this text, IMCs may be compared to 'internal notches' in the solder bulk. Notches are stress concentrators on their own account; if they are also subjected to external stresses (like the IMCs close to the two bond pads), they might be responsible for the initiation of failure (Fig. 2.6). Moreover, IMCs are believed to be responsible for dislocation coalescence and void formation leading to crack nucleation, as shown in Figs. 2.37b and 2.39b. Since ductile failures are mostly the result of microvoid coalescence [2], the propagation of fatigue cracks like those shown in Figs. 2.38 and 2.39 requires essentially the linking of these microvoids. In that sense, even the thermo-mechanical fatigue of Pb-free solders may be correlated with one of the main causes of bulk embrittlement: IMCs. Obviously, more research is required to validate the above hypothesis.

2.4.3 "Tin Pest"

Another case of possible in-service embrittlement of Sn-based Pb-free solders is the formation of "tin pest". As mentioned earlier, tin pest is a common name for

α-Sn (also known as 'grey' Sn), which is the low-temperature allotropic form of β-Sn (also known as 'white' Sn). The β-Sn-to-α-Sn transformation occurs at 13.2°C and is accompanied by a substantial volume increase of ~26% [13, 18], since the density of β-Sn is 7.31 g/cm^3 and that of α-Sn is 5.77 g/cm^3. Once started, this transformation proceeds very fast, compromising the performance of the component. Interestingly, α-Sn is more brittle than β-Sn, since it is a semiconductor and not a metal [18]; hence, the formation of tin pest qualifies as a case of embrittlement. Figure 2.40a shows samples of Sn-0.5%Cu solder, which were aged at −18°C for up to 2 years. Forty percent of the specimen surface transformed into α-Sn after 1.5 years, and this percentage increased to 70% after 1.8 years of exposure [13, 18]. Embrittlement due to tin pest might be of concern for Sn-based Pb-free solders, since these solders may essentially be considered as a dispersion of IMC particles in a nearly pure Sn matrix. The risk of embrittlement

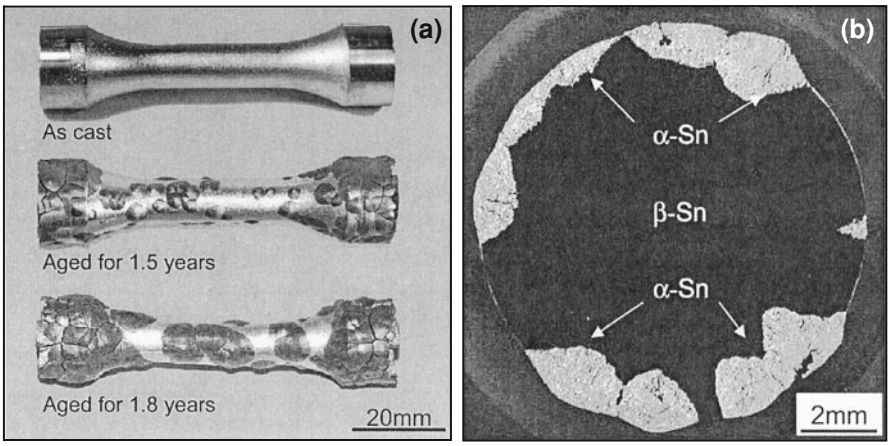

Fig. 2.40 **a** Appearance of Sn-0.5%Cu ingots aged at −18°C [13]$^{\infty}$. **b** Cross-section at the grip of a Sn-0.5%Cu sample after exposure for 1.5 years at −18°C. The tin pest formation reaction started at the surface of the sample and proceeded inwards [13]$^{\infty}$. $^{\infty}$ Reproduced with permission of Emerald Group Publishing Ltd. © 2000 by MCB University Press

Table 2.3 Tin pest-retarding effect of various alloy additions to pure Sn [18]

Alloy	Time to tin pest formation
99.998% Sn	2 h
Sn + 0.024 wt% Pb	12 days
Sn + 0.48 wt% Pb	29 days
Sn + 50 wt% Pb	190 days
Sn + 0.1 wt% Sb	14 h
Sn + 0.5 wt% Sb	Nothing visible after 5 years
Sn + 0.3 wt% Bi	330 days
Sn + 0.1 wt% Cu	4 h
Sn + 0.5 wt% Cu	7 h

becomes severe for these solders under the following two conditions: (a) the pure β-Sn grains reach the surface of the solder joint, since β-Sn transforms easier to α-Sn at free surfaces (Fig. 2.40b), and (b) the solder joint is exposed for long periods to low service temperatures. The good news is that avoiding tin pest seems to be feasible with the addition of small quantities of *tin pest retardants*, like bismuth (Bi) and antimony (Sb). Table 2.3 shows the tin pest-retarding action of various alloy additions to β-Sn specimens that have been inoculated (i.e. 'seeded') with 0.5 wt% α-Sn [18].

Acknowledgments The author would like to acknowledge certain persons, whose comments improved the quality of this text. These persons are listed in alphabetical order: Dr. Dag Andersson (IVF, Sweden), Prof. Ingrid De Wolf (imec, Belgium), Dr. Paul Michelis (IMMG, Greece), Prof. Marc Seefeldt (Department MTM, K. U. Leuven, Belgium), Dr. Geert Willems (imec, Belgium). The author also wishes to acknowledge the financial support provided by IWT (Flemish Government) in the framework of the ALSHIRA (Aspects of Lead-Free Soldering for High-Reliability Applications) Project. Last but not least, the author would like to thank Dr. B. Vandevelde, Mr. P. Limaye, and Mr. F. Duflos from imec, as well as Prof. B. Verlinden and Mr. W. Maurissen from the Department MTM of the Katholieke Universiteit Leuven (K. U. Leuven), for their collaboration on the research related with the embrittlement of Pb-free solder alloys.

References

1. Barsom JM, Rolfe ST (1999) Fracture and fatigue control in structures: applications of fracture mechanics, 3rd edn. ASTM Man Ser: MNL41, ASTM Int, West Conshohocken, USA
2. Hertzberg RW (1996) Deformation and fracture mechanics of engineering materials, 4th edn. Wiley, New York, USA
3. Hosford WF (2005) Mechanical behavior of materials, 1st edn. Cambridge University Press, New York, USA
4. Hurlich A (1968) Low temperature metals. In: Prodell AG (ed) Proc 1968 summer study supercond devices accel, pp 311–325
5. Callister WD Jr (2000) Materials science and engineering: an introduction, 5th edn. Wiley, New York, USA
6. Reed-Hill RE, Abbaschian R (1994) Physical metallurgy principles, 3rd edn. PWS Publishing Company, Boston, USA
7. Askeland DR, Phulé PP (2006) The science and engineering of materials, 5th edn. Nelson, Toronto, Canada
8. http://www.key-to-steel.com. Accessed 28 July 2008
9. Askeland DR (1984) The science and engineering of materials, 1st edn. Brooks/Cole, Monterey, USA
10. ASTM E 23-06 (2006) Standard test methods for notched bar impact testing of metallic materials. ASTM Int
11. Ratchev P, Loccufier T, Vandevelde B, Verlinden B, Teliszewski S, Werkhoven D, Allaert B (2005) A study of brittle to ductile fracture transition temperatures in bulk Pb-free solders. Proc EMPC 2005:248–252
12. Ratchev P, Vandevelde B, Verlinden B, Allaert B, Werkhoven D (2007) Brittle to ductile fracture transition in bulk Pb-free solders. IEEE Trans Compon Packag Technol 30:416–423

13. Kariya Y, Gagg C, Plumbridge WJ (2000) Tin pest in lead-free solders. Solder Surf Mount Technol 13:39–40
14. Metallography and Microstructures of Tin and Tin Alloys (2004) In: ASM Handb, vol 9: Metallography and Microstructures. ASM Int
15. Limaye P, Maurissen W, Lambrinou K, Duflos F, Vandevelde B, Allaert B, Hillaert J, Vandepitte D, Verlinden B (2007) Low-temperature embrittlement of lead-free solders in joint level impact testing. Proc EPTC 2007:140–151
16. Lambrinou K, Maurissen W, Limaye P, Vandevelde B, Verlinden B, De Wolf I (2009) A novel mechanism of embrittlement affecting the impact reliability of tin-based lead-free solder joints. J Electron Mater 38:1881–1895
17. Ratchev P, Vandevelde B, Verlinden B (2005) Effect of the intermetallics particle size on the brittle to ductile fracture transition in a bulk Sn-4 wt%Ag-0.5 wt%Cu solder. CD-ROM Proc IPC/JEDEC 10th Int Conf Lead-Free Electron Compon Assem
18. Ganesan S, Pecht M (eds) (2006) Lead-free electronics. IEEE Press, Wiley, Hoboken, USA